UNIVERSITY OF OKLAHOMA
GRADUATE COLLEGE

FLAMES AS A UNIQUE PYROLYZING SOURCE FOR THE FORMATION OF HYDROPHOBIC CARBON FILMS ON SOLID SUBSTRATES

A THESIS
SUBMITTED TO THE GRADUATE FACULTY

In partial fulfillment of the requirements for the

Degree of
MASTER OF SCIENCE

By
DUNCAN A. MERCHAN-BREUER
Norman, Oklahoma
2022

FLAMES AS A UNIQUE PYROLYZING SOURCE FOR THE FORMATION OF HYDROPHOBIC CARBON FILMS ON SOLID SUBSTRATES

A THESIS APPROVED FOR THE
SCHOOL OF AEROSPACE AND MECHANICAL ENGINEERING

BY THE COMMITTEE CONSISTING OF

Dr. Yingtao Liu, Chair
Dr. Jie Cai
Dr. Jivtesh Garg

I dedicate this Master's Thesis to my mother Sylke, my father Wilson, my sister Claudia and the countless friends and mentors who have helped me reach this point. Thank you for your unconditional support without which I would not have been able to complete this work.

Acknowledgements

I would like to express my utmost gratitude and thanks to my advisor, Dr. Yingtao Liu, who has helped support me and ensure my success as a graduate student. Dr. Liu has always believed in my capabilities as a student and a researcher. Whenever I faced a challenge or doubted my own capabilities, Dr. Liu believed in me and encouraged me to face those challenges. Without his mentorship, encouragement, and guidance I would not have been able to accomplish this work.

I am very grateful to my thesis committee: Dr. Yingtao Liu, Dr. Jie Cai, and Dr. Jivtesh Garg for not only taking the time to read, review, and approve this work; but also, for being great mentors and professors who have helped form me into the engineer I am today.

I would like to thank my colleagues in the Combustion, Plasma, and Nanoparticle Lab for the support they have provided in my six-year journey as a researcher at the University of Oklahoma. I would like to thank Ethan Murphy for introducing me to hydrophobicity research and laying the groundwork for my research, with Ethan's support and review I was able to produce publications related to hydrophobicity. I would like to thank Benjamin Berka who assisted with light microscopy analysis and helped with publication review. I would also like to thank Dr. Abdihamzehkolaei who was in the lab with me throughout my undergraduate career. Dr. Abdihamzehkolaei was a great mentor and I enjoyed spending time with him in the lab. I am grateful to Luis Carlos Mendoza Nova for continuing to work in the lab and being a coauthor on my publication, and I wish him the best of luck in pursuit of his Master's degree.

I am very thankful to Dr. Preston Larson of the Samuel Roberts Noble Microscopy Laboratory; he taught one of the most memorable classes I took at OU and instilled in me a love for electron microscopy. Furthermore, Dr. Larson provided constant support for the Scanning Electron Microscopy imaging that is critical to my research and thesis.

I would like to extend a special thanks to Dr. Elena Echeverria and Dr. David N. McIlroy from Oklahoma State University for completing X-Ray Photoelectron Spectroscopy on provided samples as well as assisting in the analysis of those results.

I would like to recognize the Gallogly College of Engineering Diversity and Inclusion Program, formerly the Multicultural Engineering Program, for their exceptional support and mentorship. I specifically wish to thank Ms. Lisa Morales, the Director of the Diversity and Inclusion Program, for her support and mentorship. When I was unsure of what I wanted to do in the future Ms. Morales was there to support me; her guidance has played a critical role in planning the next stage of my career.

The Oklahoma Louis Stokes Alliance for Minority Participation (OK-LSAMP) has played a special role in encouraging me to pursue my Master's degree. As an undergraduate student OK-LSAMP provided support and presentation opportunities for my research. I wish to thank OK-LSAMP for welcoming me into the research community and encouraging me to participate in the presentation of my research.

I would like to thank The Boeing Company for their support, flexibility, and mentorship. I started my internship with Boeing in the summer of my sophomore year and I have been very fortunate to continue my internship during the summers and as a part-time academic intern during the school year. I would like to give special thanks to my team: the B-1 Data Link Team. They have been so very accommodating and flexible with allowing me to continue working and pursuing my Master's degree; I appreciate all I have learned from them and the support working at Boeing has provided me.

I would like to give my sincerest thanks to my family: my father, mother, and sister who have continuously supported me throughout my life; I don't think there are enough words to state how grateful I am and without you I would never have been able to reach this point.

Table of Contents

Table of Figures

Table of Tables

Abstract

In this work the rapid single-step flame synthesis of hydrophobic carbon layers (C-layers) on the surface of stainless-steel (SS) substrates is explored. A co-flow flame is used to generate a hydrophobic monolayer on the surface of the metal substrate upon its insertion into the reaction zone. Several flame parameters are explored including fuel type (biodiesel and methane), exposure time of the SS substrate in the flame medium, flame position of the substrate within the flame (inner-cone vs. outer-cone), and the percent of oxygen content in the oxidizer stream. The thickness and mass of the flame formed monolayer varied depending on the various flame parameters; however, there was no significant correlation between mass of the deposited C-layer and the layer's hydrophobicity and/or uniformity. Flame structure played the most significant role in the hydrophobicity and uniformity of the deposited C-layers. It is hypothesized that a small "inner-cone" of the Canola Methyl Ester (CME) biodiesel flame along with a high soot propensity can result in an ideal medium to form uniform hydrophobic C-layers of unique hierarchical surface structure. This is supported by introducing SS substrates in methane/air flames formed using the same co-flow burner; this was further supported by experiments utilizing a CME/oxygen enriched-air flame to form C-layers.

It was found that a flame formed using a gaseous fuel (methane) over a vaporized liquid fuel, CME, has significant structural differences that enable vastly different deposition behavior of soot layers on the surface of solid substrates. Due to its larger pyrolysis zone (taller inner-cone), the CH_4/air flame has a smaller region that supports uniform soot deposition of hydrophobic C-layers compared to the CME/air flame. When a solid substrate is placed within the pyrolysis zone (inner-cone) of a flame the resulting layer is non-uniform, hydrophilic, and consists of undeveloped soot.

However, when the solid substrate is placed outside the pyrolysis zone, the deposited soot tends to be uniform and mature; ultimately creating a hydrophobic C-layer consisting of typical microscale interconnected “weblike” structures formed of spherical soot nanoparticles. The effect of oxygen content (35% and 50% O_2) in the oxidizer stream for the formation of hydrophobic C-layers was also studied in this work. It was found that oxygen enrichment within the CME flame alters the structure of the flame, hence affecting the morphology of the formed C-layer. Under oxygen enrichment the central region of the deposited C-layer is composed of a weblike structure similar to those seen in the CME/air flames; however, this central region is bordered by a region of densely compacted soot that shows signs of significant thermal stress. At 35% O_2 the thermal stress is expressed as multiple microscale cracks while at 50%O_2 this border region shows much larger cracks and macroscale layer peeling. The hydrophobic property of the carbon deposits was quantified by measuring the contact angle of water droplets placed on the film’s surface. A water droplet drop test was conducted on the flame formed hydrophobic layers to study their wettability property.

Chapter 1: Introduction[1]

1.1 Brief Research History of Wettability

The underlying wetting mechanisms on structured solid surfaces have been studied for decades. In 1936 Wenzel [1] concluded that the wettability properties of a solid substrate should be directly proportional to the physical condition (roughness) of the wetted surface. In 1944 the fundamental work of Cassie and Baxter presented the relation between the wettability of hydrophobic surfaces and the surface's roughness and porosity; in particular comparing those encountered in nature to those artificial or manmade [2]. Cassie and Baxter suggested that "water-repellency of the duck is due to the structure of its feathers" rather than to a natural water repellent agent or surface chemistry (i.e., natural oil, etc.). For instance, we know today that the ultrahydrophobicity exhibited by the lotus leaf is owed to the presence of nano and microscale architectures on its surface that promote roughness thus amplifying its hydrophobicity [3]. Two principal types of hydrophobicity, and consequently, two models were proposed [4]. The first model refers to a hydrophobic surface in which the water droplet wets the surface and is pinned. This model is known as the ***Wenzel Equilibrium state*** and occurs when the microscopic gaps of the surface structure are large enough that a water droplet's surface tension is broken under its own weight. The other model is the ***Cassie-Baxter equilibrium state*** in which the water droplet's surface tension is not broken. Instead, the droplet rests on the microscopic structures that form the surface,

[1] The content of this chapter is an extension of a published paper by the author [27, 60], co-authors have granted full authority for the reproduction of the material. The paper contains results of research which was solely conducted as partial fulfillment for the MS requirement. Materials presented in the paper have not been submitted for a course or extra credit.

creating a solid-air-liquid interface beneath the droplet. The Cassie-Baxter wetting state is a unique physical property that offers a broad range of new and exciting applications (e.g., self-cleaning, anti-smudge, corrosion resistance, etc.). The fundamental wetting properties postulated by Cassie-Baxter and Wenzel have been explored to design and develop various types of hydrophobic surfaces for a broad range of applications. Currently, products having hydrophobic surfaces are in high demand and can be found in a wide range of applications from everyday goods (e.g., stain repellants in clothing, anti-fogging, and anti-icing) to more complex systems. The application of hydrophobic surfaces can significantly help to inhibit drawbacks currently found in complex systems such as icing or frosting, heat exchangers, drag, fouling in pipes, fogging, among many others [5-9].

Briefly, the method used to determine the hydrophobicity of a surface is contact angle (CA) analysis, in which a water droplet is placed on the surface of a material and the CA of the water droplet is measured (**Figure 1**). The contact angle is defined as the angle made between the bottom of the droplet and the line tangent to the edge of the droplet at the surface liquid contact point. Materials that produce CAs greater than 90° are considered hydrophobic and materials with CAs exceeding 150° are considered superhydrophobic. Furthermore, hydrophobic and superhydrophobic surfaces can be classified into one of the two aforementioned states: the Wenzel state (a wetting state) and the Cassie-Baxter state (a non-wetting state).

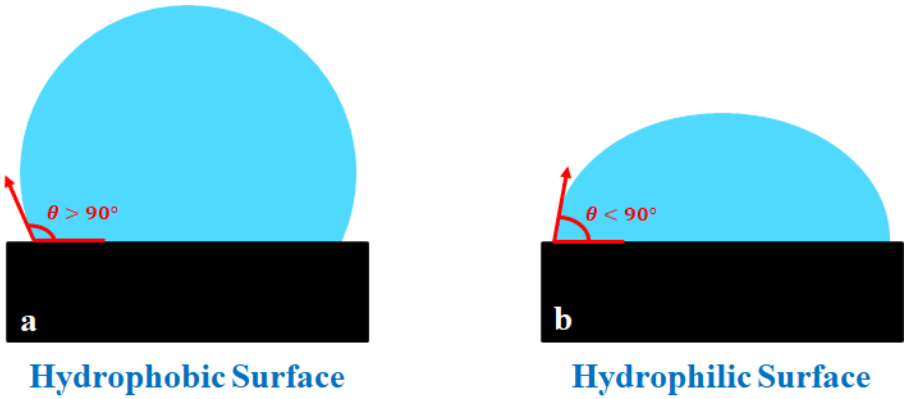

Figure 1. *Depiction of water droplet contact angles on a hydrophobic (CA* $> 90°$*) and a hydrophilic (CA* $< 90°$*) surface. The CA is measured as the angle between the bottom of the droplet and the line tangent to the edge of the water droplet.*

1.2 Typical Methods for the Formation of Hydrophobic Surfaces

Due to the unique properties and applications of hydrophobic surfaces, recent research has explored many different methods and techniques to generate superhydrophobic surfaces [10, 11]. Methods such as plasma etching, electrospinning, chemical vapor deposition (CVD), flame deposition, nanoimprint lithography (NIL), micromachining and a variety of their combinations in addition to other methods have been employed for achieving hydrophobic surfaces on various types of substrates. The plasma etching method utilizes energized gas ions in an evacuated chamber to bombard the substrate and create a rough surface [12-15] (**Figure 2(a)**). The ionic sputtering of the substrate's surface creates nanoarchitectures that ultimately give the etched substrate its hydrophobic properties. The electrospinning method utilizes a DC voltage difference between a spinneret (a syringe and metal needle) containing a colloidal suspension that is connected to a DC voltage source and a grounded substrate that is used to collect material expelled

from the spinneret (**Figure 2(b)**). Electrospinning can be used to create a hydrophobic fiber mesh on the surface of a substrate [16-20]. In CVD a sequence of chemical processes is employed to create a hydrophobic coating on the surface of a substrate (**Figure 2(c)**). The substrate is placed in the CVD chamber and a carrier gas transports gas phase precursors into the CVD chamber. Chemical reactions between the precursors and substrate create two products [21-24]. A volatile product that is whisked away by the carrier gas and a film/coating on the substrate. The flame deposition process involves placing a substrate within, or above, a flame volume and allowing soot deposits to form a thin continuous layer. Substrates of various material, geometries, and structure can be utilized. As shown in **Figure 2(d)**, a soft foil and a rigid plate can be easily coated. The deposited soot creates a rough hierarchical architecture on the substrate that imparts hydrophobic properties [25-37]. NIL uses a multistep process to create nanoarchitectures on a substrate using a pre-etched stamp (**Figure 2(e)**). A softer layer material (e.g., polymer) is heated to its glass transition temperature. Then, a pre-etched stamp is pressed into the surface of the soft material and fills the gaps within the stamp. This deforms the surface of the softer substrate and creates nanoarchitectures with the same shape characteristics as those present on the stamp [38]. Other related methods include a combination of NIL with assisted CVD [38] or sol-gel/NIL [39]. It is also possible to form hydrophobic surfaces via mechanical etching patterned microstructures on surfaces [40, 41, 7] (**Figure 2(f)**). The Jacobi group has explored the use of micromachined hydrophobic surfaces for frost prevention and deicing [42,43]. Many of the reported methods for preparing the hydrophobic surfaces require carefully designed experimental setups with specialized reagents and equipment. These methods tend to involve multi-step processes, are limited to small flat surfaces, and may be expensive and time consuming.

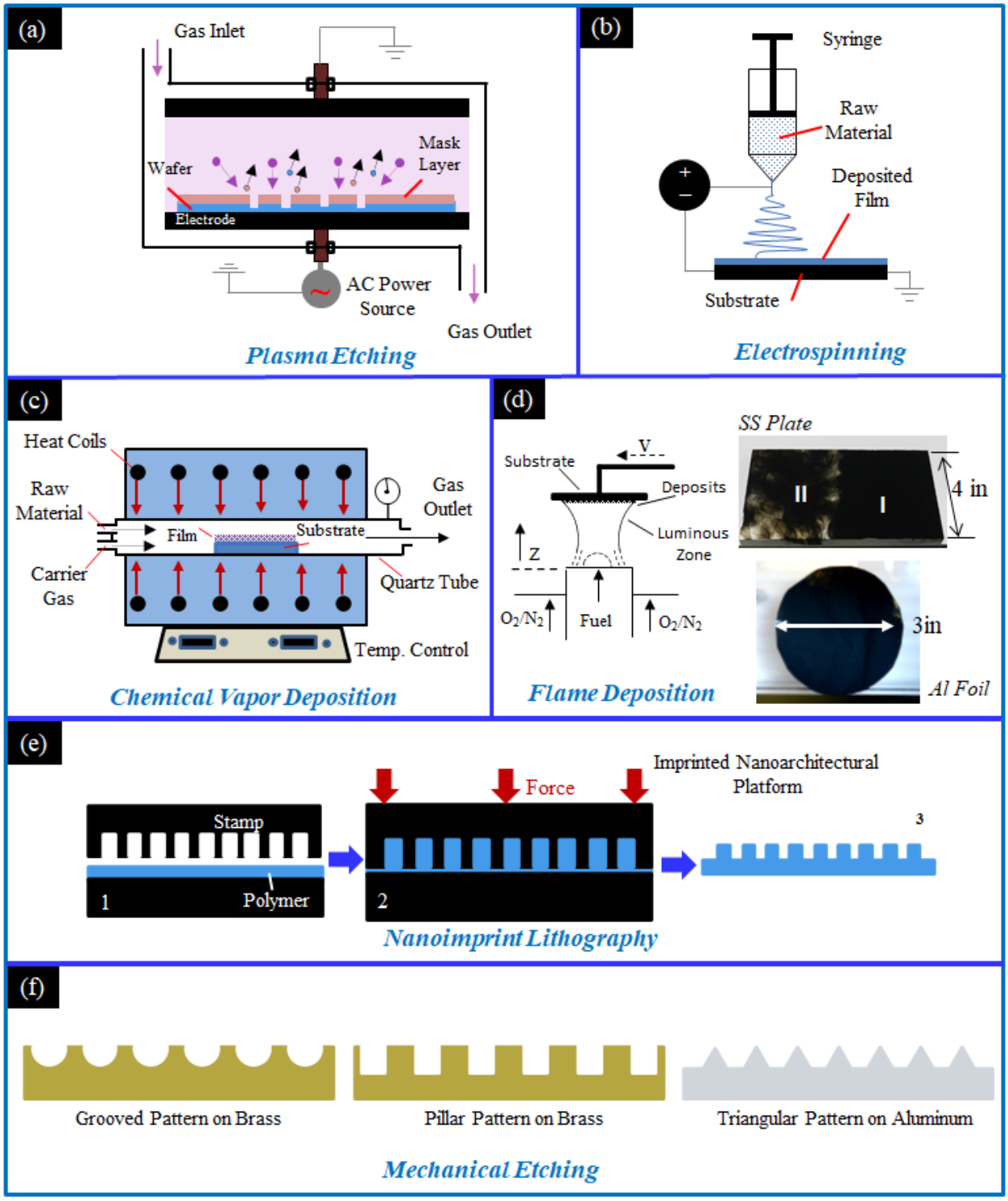

Figure 2. *Schematics of available methods to create hydrophobic surfaces: (a) the plasma etching method; (b) the electrospinning method; (c) the chemical vapor deposition method; (d) the flame deposition method; (e) the nanoimprint lithography method; and (f) mechanical etching methods.*

1.3 Various Flames Utilized to Form Hydrophobic Surfaces

Flames have been used to produce a variety of high-quality carbon nanomaterials (NMs) with unique properties and applications [44-59]. More recently, the flame deposition of hydrophobic carbon deposits onto the surface of substrates has garnered interest by researchers for further development and exploration (**Table 1**). Researchers have recognized the potential of the flame method's simple, single step process that is inexpensive, rapid, and readily scalable. The following studies have shown that a variety of different flames and deposition parameters can produce hydrophobic and superhydrophobic surfaces on substrates. As noted in this literature review, there are a variety of combustion systems to produce hydrophobic surfaces. These systems range from simple, such as a candle, to more complex and controlled systems, such as co-flow combustion burners.

Work by Naha et al. used an ethylene/air co-flow burner to form hydrophobic soot depositions on a silicon substrate [33]. It was found that different deposition areas of the flame produced layers with varying hydrophobic capabilities (**Table 1**). The morphology of hydrophobic areas was described as "spongy nanobeads" and the hydrophobic areas were located near the center of the substrate. However, depositions at the substrate edge produced hydrophilic globule like structures. The differences in hydrophobicity were attributed to oxidation of the deposits. Within the fuel cone (central depositions), the small amount of available oxygen promotes soot precursors and the formation of nanobeads that produce hydrophobic layers.

Yang et al. utilized an alcohol lamp filled with ethanol to synthesize hydrophobic materials on glass substrates; additionally flame temperature was measured at deposition areas [28]. It was determined that hydrophobicity of the deposited soot was dependent on the flame temperature, with flame temperature increasing from 672℃ at the base of the flame to 813℃ near the tip of the flame (**Table 1**). At a given flame height the temperature decreased from the flame center outwards. At all flame heights tested the outer region of the deposited soot was hydrophilic. At flame heights less than 2 cm the entirety of the deposited soot layer was hydrophilic and at flame heights greater than 2 cm the central area of deposited soot was hydrophobic (**Table 1**). The pattern of central soot deposits displaying hydrophobic qualities while outer soot deposits were hydrophilic is similar to that observed by Naha. However, unlike Naha, Yang found that both hydrophobic and hydrophilic soot depositions had similar chainlike nano- and microstructures when analyzed using SEM. The most significant difference between the hydrophobic and hydrophilic soot deposits was their grain size; a larger grain size of 50 nm for the hydrophobic deposits and a smaller 30 nm grain size for the hydrophilic deposits. The decrease in grain size may have been caused by increased rates of oxidation at the edge of the flame.

Merchan-Breuer et al. compared the hydrophobicity of carbon layers (C-layers) produced in co-flow Canola Methyl Ester (CME) and Methane (CH_4) air flames at different heights within the flame (**Table 1**). It was found that formation of the hydrophobic C-layers was highly dependent on flame structure, specifically the pyrolysis zone and the outer luminous zone [27, 60]. Deposition within the pyrolysis zone would not produce hydrophobic soot, while deposition in the luminous zone guaranteed the deposition of hydrophobic soot. It was determined that the CME/air flames,

due to being sootier and having a much smaller pyrolysis zone when compared to CH_4, are an excellent medium for the creation of hydrophobic C-layers.

Xiao et al. created hydrophobic soot layers on a glass substrate using a candle and then cleverly modifying the layer with an MTCS coating [37]. The hydrophobicity of the flame formed soot was not impacted by the MTCS layer, instead its durability was enhanced (**Table 1**): the MTCS coating improved durability of the C-layer in high temperatures, corrosive liquids, and scouring via water droplets. Furthermore, upon completion of all durability tests, the deposited soot with MTCS surface coating remained hydrophobic with only minor decreases in produced water contact angles. This illustrates the capability for flame deposition to be compatible with further enhancement by post deposition processes.

Mansurov et al. created hydrophobic surfaces using waste oil on fine and coarse river sand, showcasing the flexibility of the flame method to work on many different surfaces without using high quality fuels [34]. When water droplets were placed on the coated river sand, the water was not absorbed, instead the droplets formed unique oblong shapes that followed the curvature of the sand (**Table 1**).

Finally, Esmeryan et al. combusted rapeseed oil with air in a unique chimney burner to produce hydrophobic soot layers for anti-frosting; air was introduced to the burner at three flow rates: 0.0052 $m^3\ min^{-1}$; 0.0040 $m^3\ min^{-1}$; and 0.0030 $m^3\ min^{-1}$. It was found that at each air flow rate, 0.0052 $m^3\ min^{-1}$; 0.0040 $m^3\ min^{-1}$; and 0.0030 $m^3\ min^{-1}$, frosting occurred at temperature of $-9.8℃,\ -15℃,\ and\ -28℃$, respectively (**Table 1**). The lowest air flow rate

created soot with significantly improved anti-frosting performance that was much more durable than the other layers. Researchers attributed the performance of the soot layers to their surface morphologies. The layer formed at the highest air flow rate consisted of quasispherical aggregates that are known to be brittle, while the more durable layer formed at the lower air flow rate consisted of the more robust modified quasisquare shaped islands [29].

Some initial flame studies on the formation of hydrophobic C-layers were exploratory in nature and showcased the effectiveness and capability of these flame formed C-layers. We have expanded upon that research; first by testing two fuels, a gaseous fuel (methane) and a vaporized biodiesel fuel made of canola methyl ester (CME) to form hydrophobic carbon films on solid substrates. We have also tested the effect of oxygen enriched-air using a CME flame with 35% and 50% O_2 to form C-layers and determine the effect that increased oxygen content has on C-layer structure and hydrophobic properties. Data collected includes the mass of the C-layer, degree of hydrophobicity of the C-layer (via measuring the CA of a water droplet placed on the C-layer), identifying flame regions that resulted in the formation of a C-layer (recorded as Height Above Burner (HAB)), and the effect of time over which the C-layer was formed (recorded as substrate exposure time).

Table 1. *Schematic of various flame techniques used to create hydrophobic carbon layers.*

Author	Flame Deposition Process	Study Findings	Fuel*
Naha et al. [33]	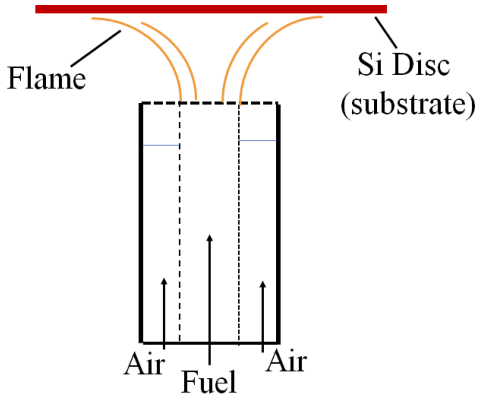	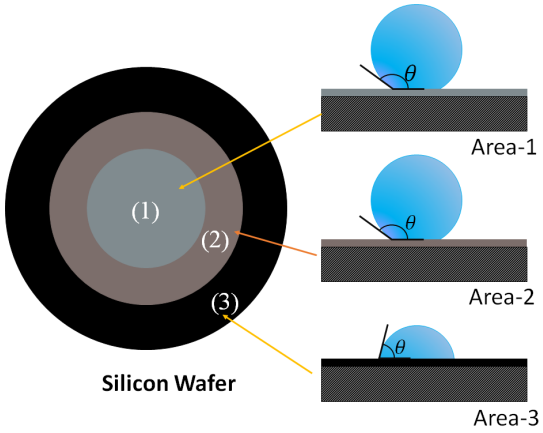	Ethylene
Yang et al. [28]	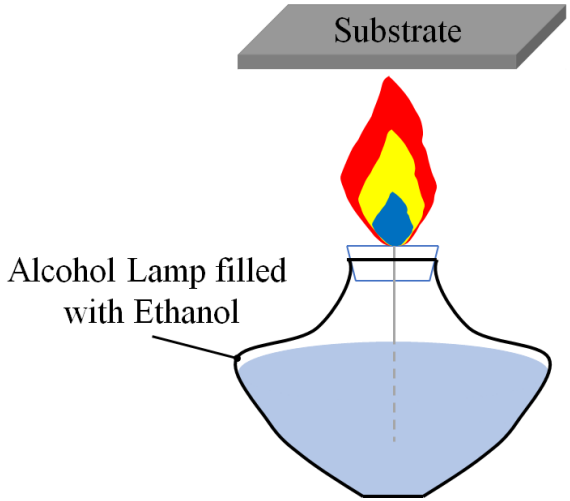	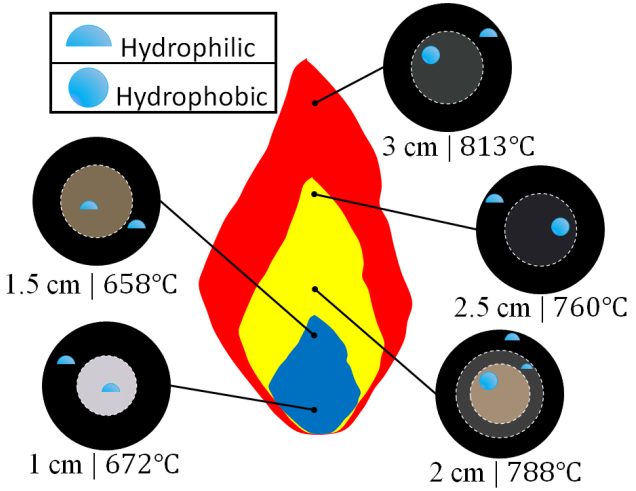	Ethanol

Author	Flame Deposition Process	Study Findings	Fuel*
Merchan-Breuer et al. [27]	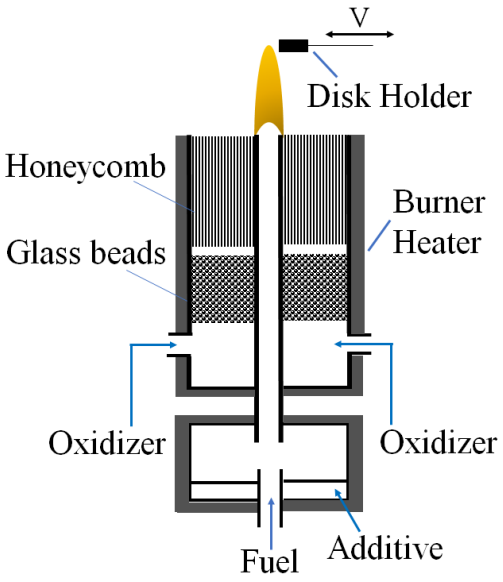	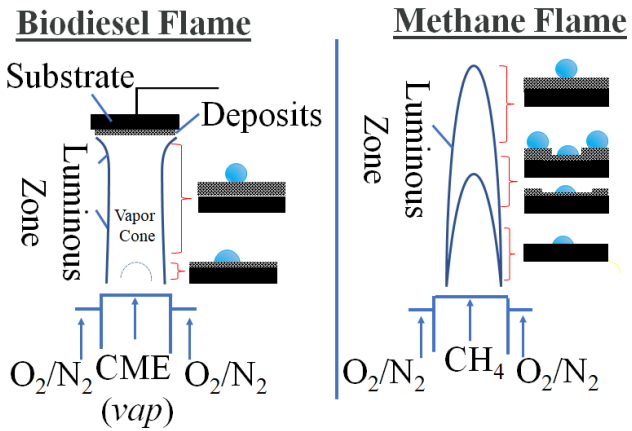	Methane & CME
Xiao et al. [37]	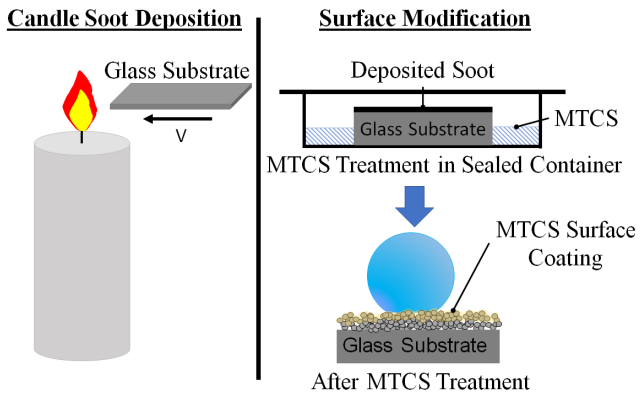	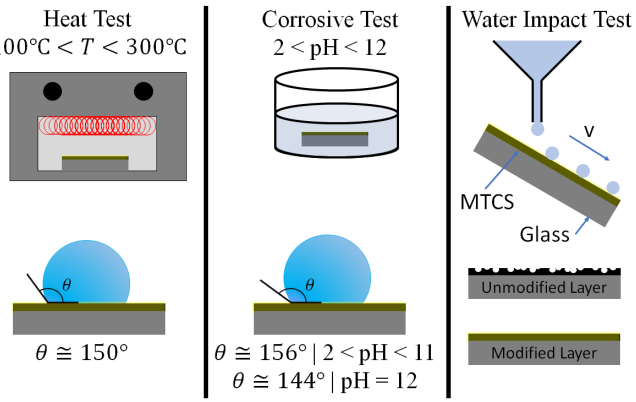	Candle

Author	Flame Deposition Process	Study Findings	Fuel*
Mansurov et al. [34]	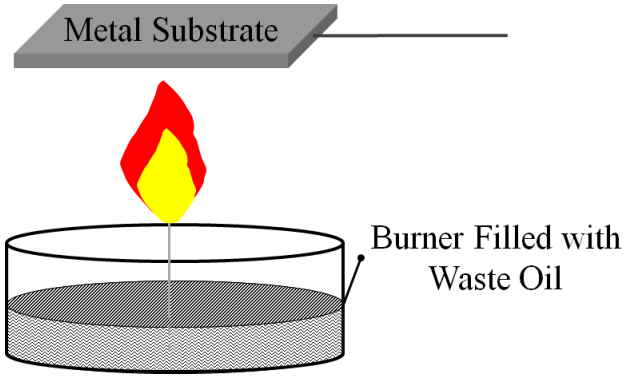	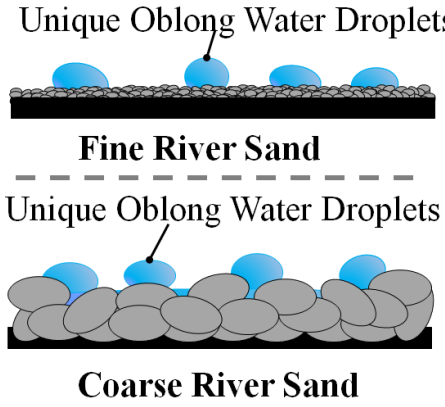	Waste Oil
Esmeryan et al. [29]	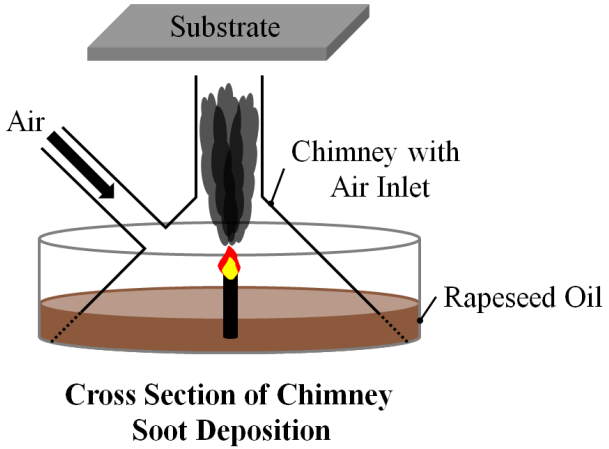	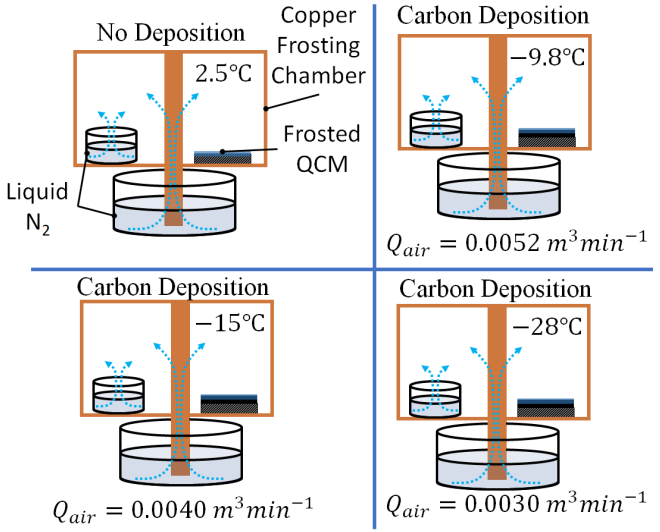	Rapeseed Oil

* Various methods utilized different fuels and combustion reactors, however, all used air as the oxidizer.

1.4 Advantages and Disadvantages of the Flame Method for Hydrophobic Surfaces

The advantage of the flame method for the creation of hydrophobic surfaces is its simplicity, rapidness, and ability to utilize it for a variety of materials of varying geometries. As shown in **Table 1**, systems as simple as a candle or a wick burner may be used to produce effective hydrophobic surfaces; more complex systems, such as burners and chimneys, can be utilized for better control of soot deposition (soot size, growth, structure, etc.). Regardless of the system used, the time required to deposit a hydrophobic film is minimal, occurring in mere minutes. Additionally, these combustion systems are able to produce hydrophobic films on a variety of materials and material geometries. Metals, polymers, glass, and even paper have all had hydrophobic C-layers successfully deposited on their surfaces. While many of these successful depositions have occurred on flat geometries, if the material can be inserted within or above a flame, a hydrophobic C-layer can be deposited on the surface.

While the flame method provides significant advantages over other methods in forming hydrophobic layers on surfaces, the formed layers tend to be very fragile. All hydrophobic surfaces will degrade with time by water contact, however, the flame formed layers are particularly susceptible to deterioration/destruction. The layer's microstructure is easily damaged via water contact; leading to a reduction in hydrophobic properties, followed by removal/delamination of the layer by water. Some other methods, such as mechanical etching (**Figure 2f**), provide a more durable hydrophobic surface, but are significantly more time, labor, and cost intensive to produce.

Researchers are further developing the flame method to produce hydrophobic films that possess improved durability (e.g., scratch/impact resistant, anti-corrosive, and anti-bacterial) [37, 61-63]. For instance, surfaces that are both hydrophobic and can maintain this property at various spectrums of the pH scale are being sought. It has been shown that some films of carbon exhibit unique combined properties: they can be superhydrophobic and also function as an ideal protective coating that suppresses oxidation of the underlying metals when exposed to corrosive fluids [64]. Feng et al. showed that a carbon film with a super hydrophobic property maintained its high CA after being exposed to corrosive solutions with pH levels ranging from 1.07 to 13.76 [64]. It is believed that graphite and graphite-like nanostructures are ideal materials for inhibiting corrosion [65]. Researchers Xiao et al. [37] have combined the flame method with polymer coatings in order to improve the deposited hydrophobic soot layer's durability in corrosive and high temperature environments, while also improving its mechanical durability and resistance to layer delamination by water impact. With further development it may soon be possible to rapidly form hydrophobic layers via flame deposition that have significantly improved durability; this would help prepare a new class of hydrophobic surfaces viable for commercial use.

1.5 Chapter Summary

This chapter described how hydrophobicity was measured (water contact angle) as well as various methods to form hydrophobic surfaces on materials (plasma etching, electrospinning, chemical vapor deposition, flame deposition, nanoimprint lithography, and mechanical etching). All hydrophobic surface synthesis methods share one common theme, they aim to roughen the material's surface on the microscale, nanoscale, or a combination of both (hierarchical

roughening). Finally, a thorough summary of literature review on various flame methods to create hydrophobic carbon deposits on a material's surface was described.

Chapter 2: Experimental Approach[2]

To create the flames for hydrophobic C-layer deposition a co-flow burner utilizing vaporized CME and gaseous methane as fuels was used. The fuels were introduced separately to investigate their effect on the formation of the C-Layers. Both CME and methane were combusted with air (O_2 = 21%); however, CME combustion also utilized oxygen enhanced combustion with oxygen contents of 35% and 50% O_2.

2.1 Co-Flow Burner

A slightly modified version of the co-flow burner developed for studying methane/ethane flames by Santoro et al. [66] is employed to create C-films on the surface of a solid flat substrate (**Figure 3**). This same burner has been used in prior research of fundamental soot formation in biodiesel and methane flames by Dr. Merchan-Merchan, Dr. Abdihamzehkolaei, and Mr. McCollam. In this work two different fuels, biodiesel (CME) and methane, were tested for generating the C-films. The burner is composed of two concentric pipes which have a diameter of 11 mm and 82 mm (**Figure 3(b)**). The central pipe is designed for supplying the fuel and the outer pipe supplies the oxidizer via four axially symmetric inlet ducts flowing through the outer channel (**Figure 3(b)**). A 3-mm diameter glass bead bed and a 51 mm thick honeycomb section (1.5 mm cell size) are used

[2] The content of this chapter is an extension of a published paper by the author [27, 60, 92], co-authors have granted full authority for the reproduction of the material. The paper contains results of research which was solely conducted as partial fulfillment for the MS requirement. Materials presented in the paper have not been submitted for a course or extra credit.

to evenly distribute the oxidizer flows inside the burner. Oxidizer flows consisting of 21% O_2, 35% O_2, and 50% O_2 were utilized.

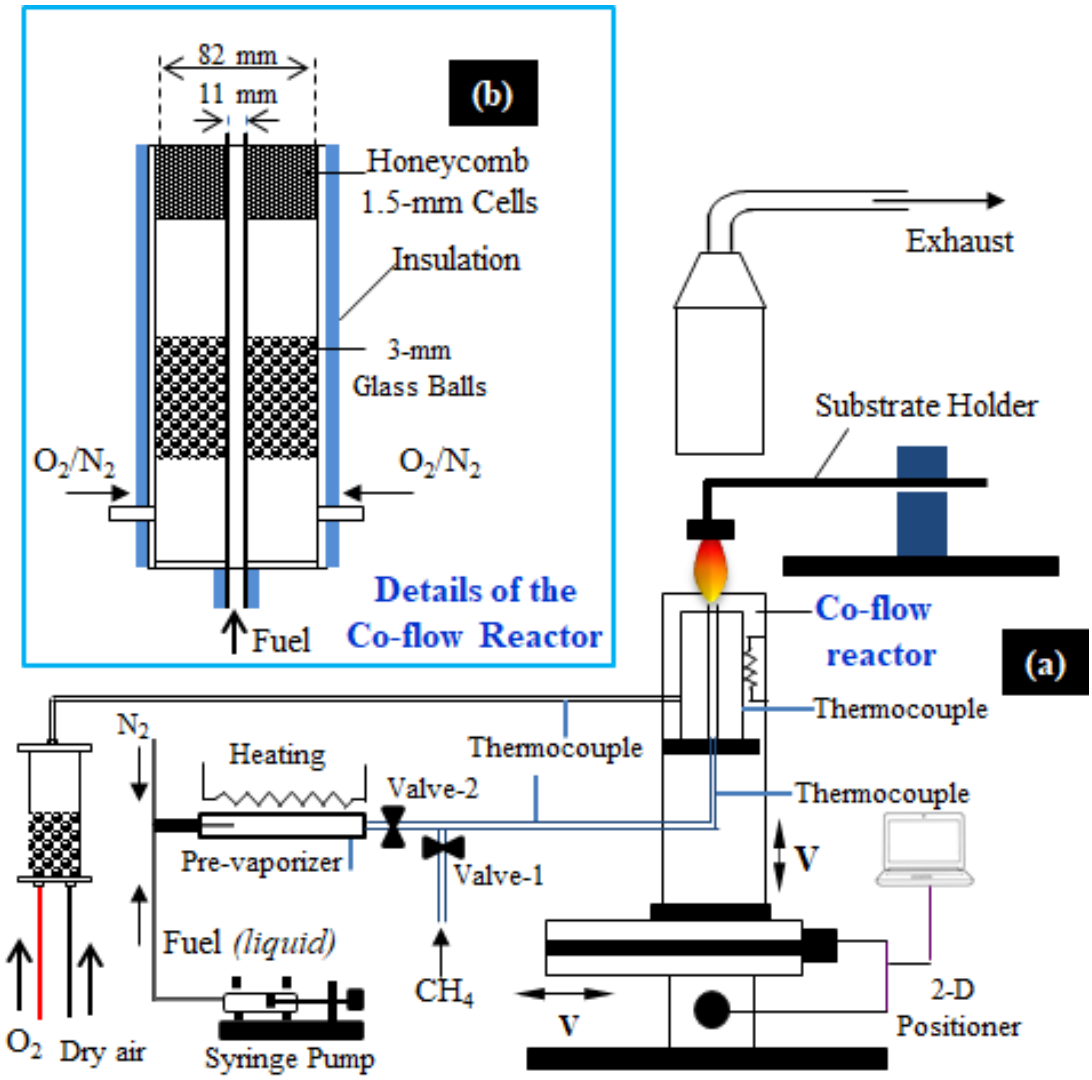

Figure 3. *Schematic of the experimental setup. (a) Mounted co-flow burner with substrate holder and (b) Detailed schematic of Co-flow Reactor.*

The tested biodiesel is canola methyl ester (CME). The biodiesel flame is formed by supplying the CME at a constant rate of 6 mL/h via a syringe pump (Model EW-74900-00 1-Channel from Cole-Parmer, Inc.). The wall of the fuel evaporator assembly and fuel line were successively heated by

an array of three heating tapes. Information about the evaporation process of the liquid fuel can be found in the literature [67]. The evaporation process of a biodiesel can cause difficulties for flame ignition and sustainability; thus, in order to stabilize the flame, it was necessary to introduce a small (<0.1 Lpm) nitrogen flow as a carrier gas into the fuel line. The CME flame was formed with valve-2 open and valve-1 closed. To form the methane flame, a methane flow rate of 0.45 Lpm was used, and valve-1 opened while valve-2 was closed. For both methane and CME an oxidizer stream at flow rate of 36 Lpm was used. The burner was mounted on a 2-D positioning system controlled by an 8300 series stepping motor controller (Model VXM-2, Velmex, Inc.). The positioner consisted of a two-dimensional unislider assembly, allowing the burner to be moved up and down as well as horizontally and vertically for optimal flame positioning [68].

Exhaust gases left the burner and entered a hood where they were funneled away from the setup. Carbon particulates were deposited onto the surface of the substrate in the form of a thin film by exposing the substrate to the flame. The flame deposition process is illustrated in **Figure 4**. The substrate used was a stainless-steel disk with a diameter of 19 mm and that disk was mounted on a 90-degree aluminum angled substrate holder (**Figure 3** and **Figure 4**). The substrate holder is mounted on an adjustable aluminum block that allows the system to move forward and backward in order to facilitate insertion into a targeted flame region. Deposits from the flame altered the surface of the SS disk into a visible black opaque surface.

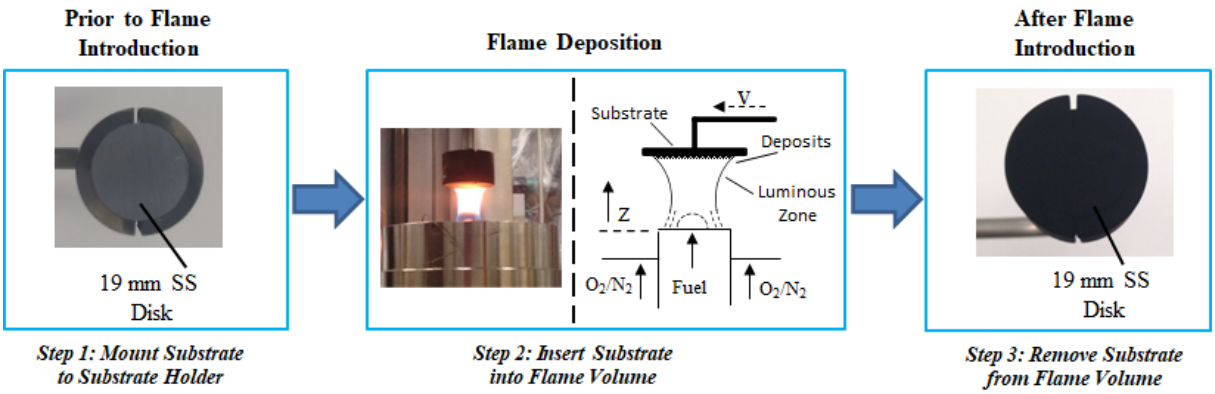

Figure 4. *Illustration of the flame deposition process. From left to right, photographs of the substrate holder before, during, and after flame deposition are shown. The diagram provides a schematic of the soot deposition process.*

Stainless steel disks were used due to their resistance to high temperatures and their ability to be easily placed and held within the substrate holder. Additionally, the CH_4/air and CME/air flames' temperature profiles were measured using an Omega R-Type thermocouple. After the substrate was inserted into the flame volume, the collected soot layer's surface morphology was analyzed using a light microscope (Stemi SV 11). Detailed structural and chemical characteristics of the flame formed carbonaceous structures were obtained using scanning electron microscopy (SEM) (Zeiss Neon-40 EsB FIB-SEM), transmission electron microscopy (TEM) (JEOL TEM-3010), SEM-X-ray energy dispersive spectroscopy (SEM-EDX) (INCA Energy 250) and X-ray photoelectron spectroscopy (XPS). For confirming the physical characteristics of the carbonaceous particulates observed in the SEM images, TEM analysis was conducted by collecting samples near the positions where the SS disks were introduced into the flame. For TEM analysis, soot samples were collected thermophoretically from the center of the flame by the impaction of particulates

onto the carbon-coated copper grids (EMS, Inc). X-ray energy dispersive spectroscopy and XPS provides chemical information of the bulk soot and its surface, respectively.

2.2 Tested Flame Parameters

Various parameters were tested in this flame deposition method for the synthesis of hydrophobic surfaces. These parameters included: fuel type, flame position, substrate (SS disk) exposure time inside the flame, and percent of oxygen within the oxidizer stream. A description of tested parameters is listed in **Table 2** and photographs of the CME and CH_4 flames are presented in **Figure 5**. The SS disk-flame interaction allowed for carbon particulates to be deposited onto the substrate's surface and form a C-layer. In Flame I, the SS substrate was inserted into the CME/air flame at varying heights above the burner (HAB) (10, 12, 15, and 20 mm) for a substrate exposure time of 5 minutes. The total length of the CME/air flame is approximately 22 mm. In Flame II, the substrates were inserted into the CME flame at a height of 15 mm HAB for varying periods of time (2, 5, and 10 minutes) to study the effect of substrate exposure time. Flame III was a CH_4/air flame with a height of approximately 85 mm. The substrate was inserted into the flame at heights of 50 and 60 mm for an exposure time of 1 min. Two flames were studied for the effect oxygen-enhanced combustion had on the deposited C-layers. Both flames utilized CME as the fuel and the oxygen content within the oxidizer stream was increased to 35% and then 50% O_2 (N_2 made up the balance of the oxidizer). The substrate was inserted into the flame volume at approximately three-quarters the flame height for an exposure time of 5 minutes for 35% and 50% O_2. Flame IV (35% O_2) was ~12 mm in height and the substrate was inserted at ~9 mm HAB. Flame V (50% O_2) was ~10.6 mm in height and the substrate was inserted at ~8mm HAB.

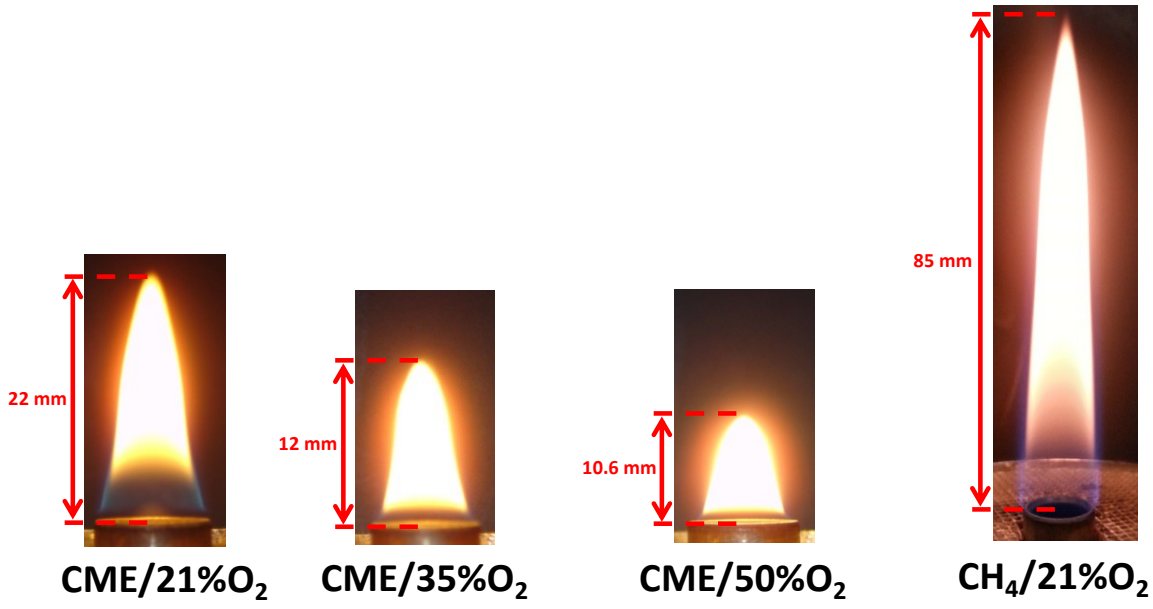

Figure 5. *Photographs of the CME/air, CME/35%O_2, CME/50%O_2, and the CH_4/air flames are shown. In the CME flames the increase in oxygen content was accompanied by a decrease in flame height. The CH_4/air flame was the tallest flame used for flame deposition.*

The flame treated substrates underwent a water droplet test to determine the hydrophobicity of the deposited carbonaceous materials through contact angle (CA) analysis. The contact angle, θ, is measured at the point of contact of two hypothetical lines between the liquid droplet and the solid C-layer. One horizontal line is parallel to the solid surface (C-film) and the other is tangent to the edge of the droplet. Photographs were collected and imported into a computer where the contact angle of the droplet was measured using digital micrograft software.

Table 2. *Description of the various flame parameters used for C-layer deposition.*

Flame	Fuel	*HAB (mm)*	*Exposure Time (min)*	*Oxidizer (% O_2)*
Flame I	CME ($C_{19}H_{36}O_2$)	10, 12, 15, 20	5	21
Flame II	CME	15	2, 5, 10	21
Flame III	Methane (CH_4)	50, 60	1	21
Flame IV	CME	9	5	35
Flame V	CME	8	5	50

2.3 Variations in Flame Structure

Flame structure is a significant factor for the formation of C-layers and their hydrophobic properties. Both the CME/air and CH_4/air flame are composed of two dominant color characteristics; a region in the upper part of the flame where an intensive yellowish luminous zone (soot thermal radiation) is present and a lower region that is clear or a pyrolysis zone (**Figure 5** and **Figure 6**). In the CH_4/air flame the pyrolysis zone (flame "inner-cone") is much longer compared to the CME/air flame (**Figure 6**).

CME and methane are both carbon-based organic products extracted from different sources. The combustion of these two fuels can result in flames of very different properties. Some of the properties relevant to this study include flame temperature, soot propensity and flame structure. CME ($C_{19}H_{36}O_2$) is composed of a variety of constituents including methyl palmitate (5% $C_{17}H_{34}O_2$), methyl stearate (3% $C_{19}H_{38}O_2$), methyl oleate (62% $C_{19}H_{36}O_2$), Methyl linoleate (20% $C_{19}H_{36}O_2$) and methyl linolenate (10% $C_{19}H_{32}O_2$) [69]. The content of constituents in a fatty acid methyl ester varies according to the feedstock employed and can significantly affect the physical,

chemical, and fuel properties [70, 71]. In general biodiesel contains approximately 11% oxygen by weight and lacks aromatic compounds [72, 73, 74]. Methane is the simplest alkane (C_nH_{2n+2}, where n is equal to one) and is an acyclic saturated compound while CME is principally composed of unsaturated fatty acids. Soot propensity has been studied using two very distinct type of fuels in droplet combustion by Li et al [70]. In that study the soot propensity of biodiesel and hexadecane ($C_{16}H_{34}$) were compared. Li et al. found that hexadecane produced practically no soot and the flame was almost completely blue. However, the biodiesel flame was much sootier and displayed a larger luminous zone. These findings are corroborated in our study.

Furthermore, the oxygen-enhanced combustion of CME produced a unique flame structure; in contrast to the CME/air and CH_4/air flames, the CME/oxygen-enhanced (35% O_2 and 50% O_2) flames produced a barely discernable pyrolysis zone that was only visible at the burner inlet/base of the flame (**Figure 5** and **Figure 6**). Alteration of the flame structure allows for the modification of deposited soot, ultimately affecting the properties (mass, hydrophobicity, stability, etc.) of the deposited C-layer. Leveraging this improved control of the flame deposits' properties may allow for the creation of highly customizable C-layers that meet specific requirements of mass, thickness, hydrophobicity, and stability without requiring post deposition processes.

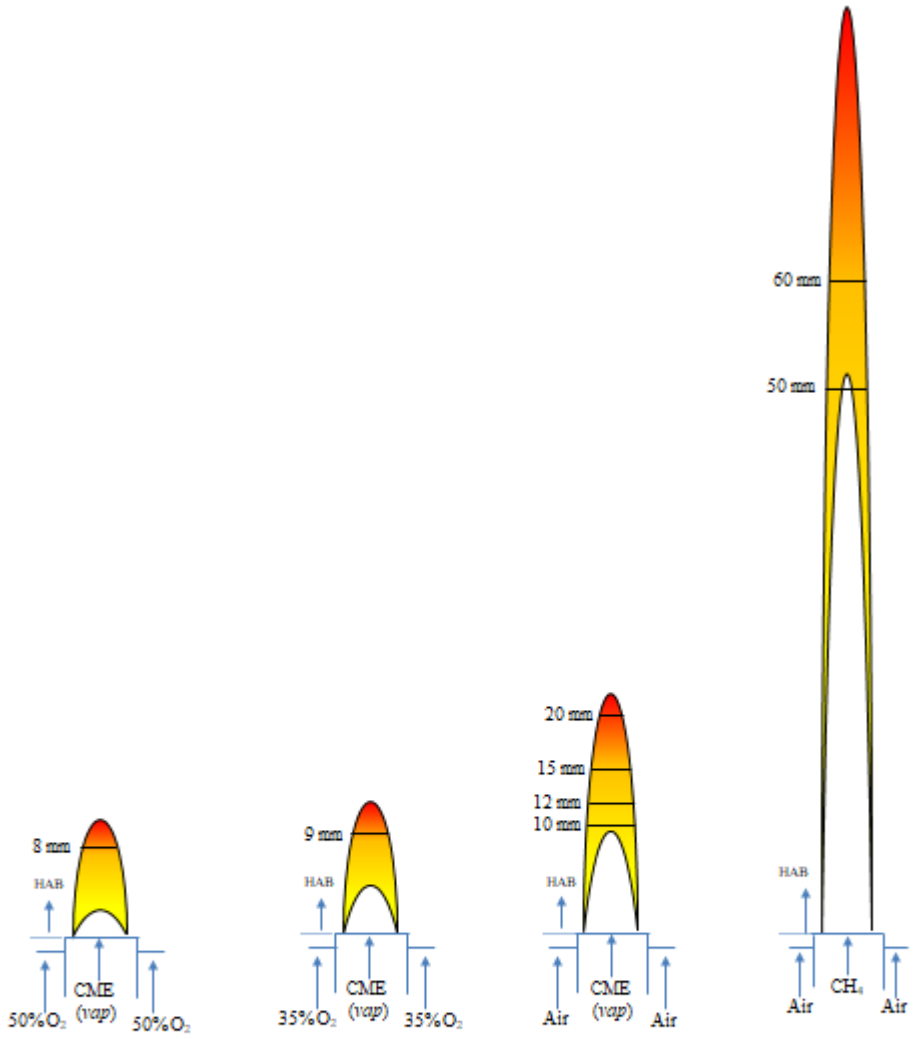

Figure 6. *Diagrams of the CME/50%O_2, CME/50%O_2, CME/50%O_2, and CH_4/air flames. The luminous zone and inner flame are depicted by the colored and whitespace areas of the flame, respectively. Insertion heights of the substrate into the flame for C-layer deposition are labeled on the respective flame. Flame heights are drawn to scale.*

2.4 Imaging and Analysis Techniques Utilized

Images and data for analysis were captured using light microscopy, TEM, SEM, SEM-EDX, XPS, and a high-speed camera. A light microscope and SEM were utilized to characterize the surface of the deposited C-layers as these imaging techniques are focused on external/surface level analysis. Using TEM, for select samples, it was possible to view the internal structure of captured soot particulates from regions of the flame where C-layers were formed, allowing for the characterization of soot growth and maturity within given flame regions. Furthermore, SEM-EDX and XPS were used to determine chemical/atomic properties of the deposited layers' surface. SEM-EDX provides a concentration of elements present of the surface of a material while XPS provided details of chemical bonding and the lack of complex functional groups present on the surface. Finally, a high-speed camera was used to showcase the capabilities of the deposited layer to repel water; specifically, when water was dropped from a distance above the C-layer it would bounce across the surface instead of wetting the layer.

It is important to note that electron microscopy (SEM and TEM) provides much higher resolution than light microscopy due to the illumination source. As stated by Abbe's Equation, in a perfect lens imaging system, the diffraction-limited resolution (d_0) is given by Equation 1, where λ represents the wavelength of the illumination source and $n \sin(\alpha)$ is the numerical aperture (a property of the microscope).

$$d_0 = \frac{0.612\lambda}{n \sin(\alpha)} \quad (1)$$

As can be seen, the resolution is limited by the wavelength of the illumination source (assuming the numerical aperture is held constant). The wavelength of visible light ranges from 400 nm to

700 nm. SEM/TEM utilizes electrons as the light source and the wavelength of the electron can be defined using the DeBroglie wavelength equations as shown in Equation 2, where h is Planck's constant, m is the mass of the electron, and v is the velocity of the electron.

$$\lambda = \frac{h}{mv} \tag{2}$$

Utilizing conservation of energy and Equation 2, the wavelength of an electron can be given as a function of voltage (as shown in Equation 3). This voltage (V) is known as the accelerating voltage in electron microscopy.

$$\lambda = \frac{1.23}{\sqrt{V}}\ nm \tag{3}$$

As shown in Equation 3, as the accelerating voltage of the electron microscope increases the wavelength of the electrons will decrease; in combination with Equation 1 this shows that as accelerating voltage increases the ultimate resolution will improve (d_0 decreases) as shown in Equation 4. The following simplifications and assumptions have been made: (i) due to electron microscopy occurring in a vacuum, $n = 1$; (ii) α is relatively small, in which the following holds true $\sin\alpha = \alpha$; and (iii) constants have been multiplied and rounded.

$$d_0 = \frac{0.753}{\alpha\sqrt{V}}\ nm \tag{4}$$

By increasing the accelerating voltage, electron microscopy can easily surpass the resolution limit of light microscopes. Equation 4 also provides insight on why TEM has better resolution than SEM; TEM is able to utilize higher voltages than SEM. Commonly used SEM accelerating voltages range from 5kV – 30 kV, while TEM accelerating voltages easily exceed 100kV and can reach 300 kV [75-78].

2.4.1 Light Microscopy

The light microscope used in this study was a Stemi SV 11. Light microscopy is a direct imaging technique that utilizes light as an illumination source to capture an image. The light is focused through a series of lenses to capture magnified images of a sample. The sample is placed on a stage and a backlight is used to illuminate the sample; once properly illuminated the focus was adjusted and an image captured and saved to a computer.

2.4.2 SEM and SEM-EDX

The Scanning Electron Microscope used in this study was a Zeiss Neon-40 EsB FIB-SEM and the SEM-EDX system was the INCA Energy 250. Scanning Electron Microscopy utilizes an electron beam to capture scanned images of a sample's surface. This image is not captured directly, instead sensors in the SEM use software to construct an image of the sample from signals released by electron beam-sample interactions. In this way, SEM is not a direct imaging technique like light microscopy or TEM but more comparable to a signal measuring technique. In a SEM a sample is placed within an evacuated chamber and impacted with a beam of electrons; a vacuum is required in order to minimize the electron beam interacting with other molecules that would create noise. Electrons impact and interact with the sample; two primary types of electrons are released via this interaction: backscattered electrons (BSE) and secondary electrons (SE). In the case of the present research, BSE imaging was not used; BSE imaging is primarily used to image differences in material composition (e.g., aluminum vs copper would appear as different contrasts in BSE imaging). Secondary electron imaging was heavily utilized as this type of imaging displays

differences in topography. As the electron beam scans across the sample, secondary electrons are created and released. A special sensor/detector within the evacuated chamber attracts these electrons using a small charge and records the electron energy. Using the recorded energy and software, a topographical map of the scanned surface is generated on the computer and this image is saved as the SEM image [79, 80].

While SEM imaging utilizes secondary electrons to form a topographical image, SEM-EDX utilizes X-rays released by the electron beam interaction with the sample to determine the elemental makeup of the sample. To accomplish this, SEM-EDX utilizes a more energetic electron beam than typical SEM image analysis. When the more energetic electron beam interacts with the sample it will begin "knocking off" electrons from atoms on the surface of the sample. As these electrons are "knocked off" from inner (low energy) electron shells they will be replaced by electrons from outer (high energy) electron shells. When electrons move from a higher energy state (high energy outer shell) to a lower energy state (lower energy inner shell) energy is released in the form of an X-ray. Sensors within the SEM chamber will measure the energy of the released X-ray and based on that energy measurement the element can be determined – allowing for the determination of the sample surface's elemental makeup [80].

2.4.3 TEM

The Transmission Electron Microscope used in this study was a JEOL TEM-3010. Transmission Electron Microscope imaging shares many similarities with light microscopy as these are both direct imaging techniques where the illumination source (light for light microscopy and an electron

beam for TEM) interacts directly with the sample and is used to project an image; for a light microscope this image is projected on the eye of the user and for TEM this image is projected onto a fluorescent screen. Due to the use of an electron beam, the samples being analyzed with TEM need to be placed in an evacuated chamber to prevent the electrons interacting with other material. Furthermore, due to the direct imaging nature of TEM the samples need to be very thin, this will allow for the electrons to "pass through" the sample. Once the electrons interact and pass through the sample, the electrons create an image that is magnified using a series of electro-magnetic lenses and the final image is projected onto a fluorescent screen; this fluorescent projection is what the TEM user ultimately views. Images projected onto the fluorescent screen are captured and saved. Due to the nature of TEM imaging utilizing electrons that "pass through" a sample, TEM provides not only high-resolution imaging but also allows for internal structures of a sample to be imaged [81].

2.4.4 XPS

The X-Ray Photoelectron Spectroscopy system used in this study was the Physical Electronics XR 04-548. X-Ray Photoelectron Spectroscopy is used to determine the chemical properties of a sample's surface. Similar to SEM and TEM techniques, XPS requires the sample be placed in an evacuated chamber. An X-ray is used to excite the sample's surface which releases electrons; the energy of the released electrons is measured and recorded. From the collected data a spectrum is created that shows the number of electrons released at a given binding energy. This allows researchers to determine the type of elements present at the sample's surface as well as the type of bonding between elements [82].

2.4.5 High Speed Camera

The high-speed camera used in this study was the MotionPro X3. High-speed cameras are used to study objects in motion that are too fast to capture with a standard camera. With a high-speed camera thousands of images can be collected in seconds; this allows researchers to determine how an object in motion interacts with its surroundings. In the presented research a high-speed camera was used to determine how a water droplet dropped from a set height interacts with a C-layer; that is a water droplet in motion interacting with a hydrophobic flame formed surface.

2.5 Thesis Objectives

The objective of this study is to analyze and discuss the capability and mechanism of flames as an efficient pyrolyzing carbon source for generating hydrophobic carbon layers. At the end of this work the following elements of hydrophobic flame formed C-layers will have been addressed:

- Hydrophobic properties of flame formed C-layers are conferred by the layer's unique hierarchical surface structure that displays both nano and microscale roughness.
- Structures of the C-layer are formed by carbon particulates that are carried by the flame's gas flow and travel towards the tip of the flame where they are deposited on a solid surface to form a C-layer.
- The C-layers formed on the substrates are highly dependent on flame structure and insertion parameters of the substrate. By adjusting the fuel type, oxidizer, insertion height

of substrate into the flame, and exposure time of substrate within the flame the deposited C-layer can be significantly modified.

- The structure of the flame plays a significant role in the formation of the C-layer, specifically the role of the “inner-cone” and “luminous zone”. Within and near the inner-cone hydrophobic carbon deposits are not formed due to this being the area of young undeveloped soot. The luminous zone of the flame, however, is an ideal region to form hydrophobic layers due to the presence of mature and more developed soot that has already formed long interconnected branches.

Chapter 3: CME/Air Flame Formed Hydrophobic Layers[3]

3.1 Effect of Substrate Insertion Height for C-layer Deposition

Figure 7 shows the characteristics of the surface morphology of C-layers formed on the surface of a SS substrate positioned at various heights above the burner (HAB) in a laminar co-flow diffusion vaporized CME/air flame. The hydrophobic/hydrophilic properties of the C-layers for this flame condition were studied through measurements of the CA (**Figure 7**). The SS substrates were inserted at various HABs of 10, 12, 15, and 20 mm for an exposure time of five minutes. The SS substrate positioned at 10 mm HAB was just above the "inner-cone" of the flame (boundary between the pyrolysis and luminous zones). Scanning electron microscopy (SEM) analysis on the surface of condensed-phase deposits shows details of the morphology of the deposits that formed the C-layers (**Figure 7(a1-a2, b1-b2, c1-c2, d1-d2)**). The photographs (**Figure 7(a7, b4, c7, d7)**) show the contact angle of a water droplet placed on the surface of the C-layer at each corresponding height. From the measurements of the water droplet's CA, it can be observed that the C-layer formed at 10 mm HAB was hydrophilic due to a CA less than 90 degrees ($\theta a = 76°$) (**Figure 7(a7)**). The C-layer thickness increased as the position of the SS substrate increased in distance from the exit port of the vaporized fuel. The mass of each SS substrate was measured before and after exposure to the flame medium. At a HAB of 12, 15, and 20 mm (within the yellow luminous flame region) the mass of the layers formed on the surface of the SS substrates was measured as 1.0, 5.0

[3] The content of this chapter is an extension of a published paper by the author [27, 60], co-authors have granted full authority for the reproduction of the material. The paper contains results of research which was solely conducted as partial fulfillment for the MS requirement. Materials presented in the paper have not been submitted for a course or extra credit.

and 9.0 mg, respectively. C-layers formed at these flame positions are all hydrophobic, showing that once a C-layer reaches a morphology that favors hydrophobic properties the mass of the layer does not significantly affect the CA. In **Figure 7** we can observe that C-layers formed at HABs of 12 mm and greater possess hydrophobic and superhydrophobic properties despite the differences in their mass. The mass of the C-layer formed at HAB of 12 mm is ~5 times less than that of the substrate positioned at 15 mm. However, the CA does not vary proportionally to the mass difference (**Figure 7(b4, c7)**).

When the SS substrate was positioned near the tip of the flame (20 mm HAB) the mass of the C-layer is ~ 9 times that of the C-layer formed at 12 mm HAB, and is almost double than that formed at the 15 mm HAB. Once again, the large mass difference does not apply a proportional impact on the measured CA. It is evident that the thickness of the C-layer increases as the substrate is positioned higher in the flame, however the degree of hydrophobicity does not deviate significantly **Figure 7(b4, c7, d7)**. A simple inspection of the SEM images in **Figure 7** reveals that the surface morphology of the carbon deposits formed at various flame heights, within the luminous zone (above the flame cone), exhibit minor variations.

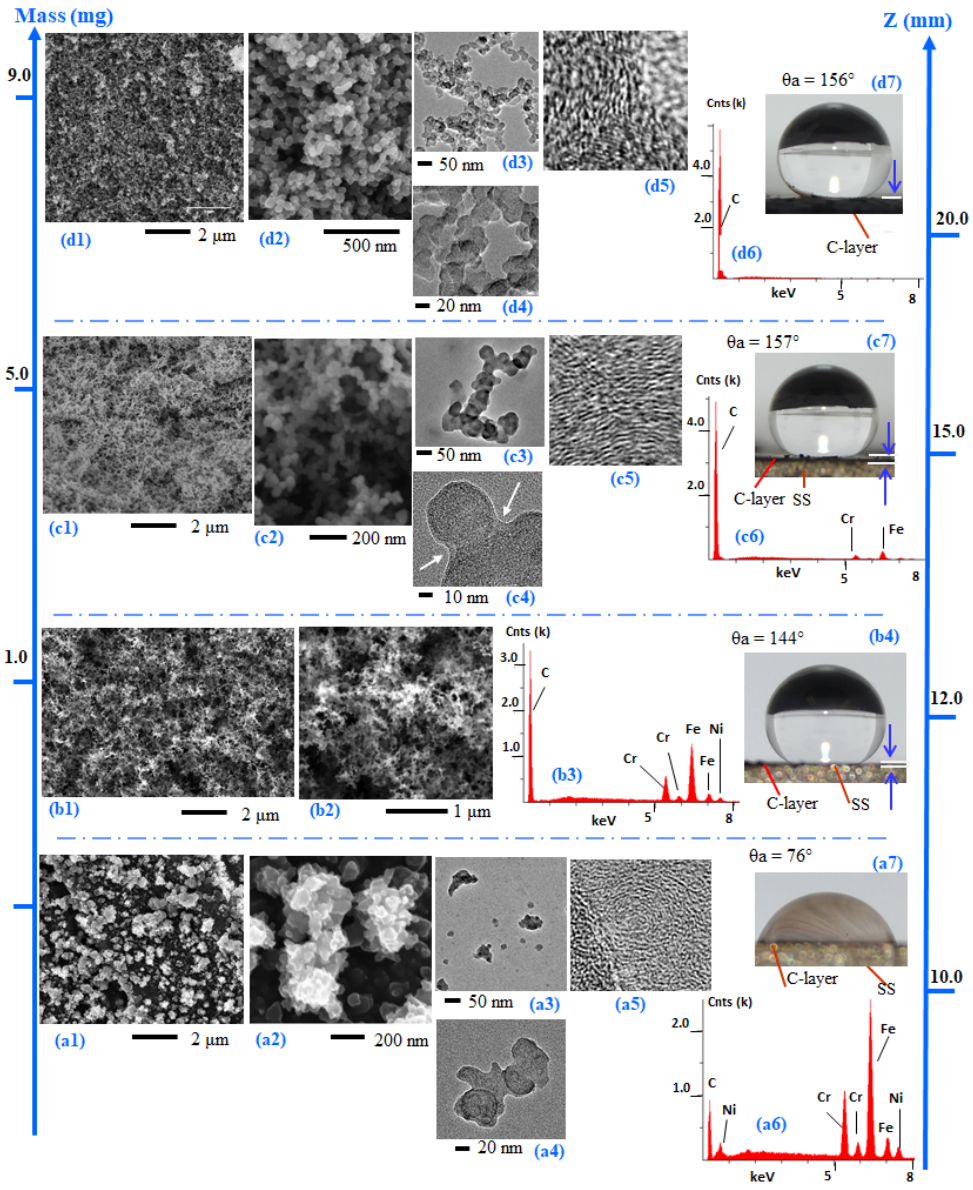

Figure 7. *Hydrophobic surfaces formed on the surface of SS substrates inserted in a CME/air diffusion flame at various heights above the burner (HAB) for a five-minute exposure time. SEM images (left images) show the morphological details of the layer's surface; the EDX spectra (a6, b3, c6 and d6) show the bulk chemical composition of the C-layers; the TEM analysis samples of soot particulates were collected thermophoretically by introducing TEM grids near the positions where the SS disks were introduced into the flame; the photographs (right photo images) show the static contact angle of a water droplet on the surface of the corresponding layers.*

However, a substantial variation in the C-layer morphology is observed between the SS substrate positioned at 10 mm HAB (within the flame cone) compared to those formed on substrates inserted in the upper flame region where the flame has a yellow luminous appearance due to the strong emission characteristic of soot radiation. SEM analysis shows that the C-layers formed in the yellow luminous zone of the flame appear to be composed of typical agglomerated sub-micron aggregates. As shown in **Figure 7(b1, b2)**, the carbon aggregates formed at 12 mm HAB are long, fine and interconnected; resembling "carbon webs" or "spiderweb-like" structures. The elongated aggregates are composed of fused primary carbon particles (nanoscale size) that have a nearly spheroidal shape. Furthermore, the unique structures found at a HAB of 12, 15, and 20 mm are hierarchical in nature; they are microscale architectures with finer nanoscale details (**Figure 7(b1-d1, b2-d2)**). The C-layer formed at 10 mm HAB appears to be composed of irregular "granular-like" deposits (**Figure 7(a1-a2)**). High resolution SEM imaging of these deposits shows that they are formed of individual spheres that are clumped together (**Figure 7(a2)**). The presence of long interconnected aggregates formed of nanometer scale primary soot particles is not present in this C-layer, and a water droplet placed on its surface shows that the C-layer is hydrophilic (**Figure 7(a1, a2, a7)**). The stark contrast of the surface morphology of the C-layer at 10 mm HAB is not surprising since this is the region of soot inception [83]. At the HAB of 10 mm the difference in mass of the SS substrate before and after its insertion into the flame was not detectable with our digital scale, and hence is not displayed in **Figure 7**. TEM imaging analysis matches the SEM results that the morphological characteristics of the soot aggregates are composed of particles that are nearly similar before and after deposition. A comparison of the TEM analysis of samples collected from a lower region (**Figure 7(a3, a4)**) to the upper region (**Figure 7(d3, d4)**) of the

biodiesel/air flame shows the transition from polydisperse size distribution “irregular-shaped” droplet-like soot precursors to a more monodispersed size small-particle morphology. In the intermediate and upper regions of the flame it can be observed that soot agglomerates are composed of tens of nanosized primary particles that are approximately spherical-shaped. It is notable that the sizes of the “irregular-shaped” liquid-like deposits present at the lower region of the flame (close to the fuel nozzle) are much larger than those of the mature soot particles present in the upper flame region. The “irregular-shaped” liquid-like deposits are building blocks of the C-layers with rough morphologies. These large “irregular-shaped” droplet-like deposits are believed to be condensate phase soot precursors [84]. Applying HR-TEM to selected primary particles collected from the different flame zones along the axial direction of the CME/air flame reveal that the soot has some type of crystallinity. Soot deposited near the flame root appears to be composed of segments of small graphene layers that are concentrically stacked and surrounded with a layer of tar-like material (**Figure 7(a5)**). This tar-like or amorphous material allows for the particles to easily fuse and form larger particles. In contrast, soot composed of more well-defined crystallites, or so called graphitic inner structures, are evident in the intermediate and mature stages present in the upper regions of the flame (**Figure 7(c5, d5)**). The necking of the primary particles fused to form the aggregates is evident in the HR-TEM images as pointed out with the arrows in **Figure 7(c4)**.

X-ray energy dispersive spectroscopy analysis conducted on the as grown C-layers in the CME/air flame shows that the C-layers consist predominantly of carbon with minor instances of oxygen. Instances of Cr, Fe, and Ni are attributed to the SS substrate. **Figure 7(a6, b3, c6, d6)** represent EDX analysis conducted on the as grown C-layers from the CME/air flame as a function of probe

position (HAB of 10, 12, 15 and 20 mm) at a fixed substrate exposure time (5 minutes). The Cr, Ni and Fe peaks decrease as the HAB of the SS disk is increased, which is interpreted as a thickening of the C-layer. The "bulk" chemical compositions (EDX analysis) of the carbon deposits formed at 10, 12, 15, and 20 mm HAB show O contents of 1.33 atomic percentage (at.%) (**Figure 7(a6)**), 0.25 at.% (**Figure 7(b3)),** 1.42 at.% (**Figure 7(c6)**) and 2.17 at. % (**Figure 7(d6)**). The EDX spectra show that the C content for the 10, 12, 15, and 20 mm HAB is ~81.28 at.%, 94.97 at.%, 97.62 at.%, and 97.76 at.%, respectively. As the SS substrate is lowered in the flame height, the O at. % decreases then suddenly increases as we move towards the base of the flame. The O at. % is higher at the lowest tested region of the flame (HAB = 10 mm) compared to the HAB = 12 mm. This can be attributed to CME being an oxygenated fuel.

3.2 Effect of Substrate Exposure Time for C-layer Deposition

The morphological properties and hydrophobicity of the deposited carbonaceous materials were also studied by varying the SS disk exposure time. Experiments were conducted using the CME/air flame and varying the substrate exposure time. C-layers were collected at substrate exposure times of 2, 5, and 10 minutes at a fixed HAB of 15 mm (**Figure 8**). The photographs (**Figure 8**) demonstrate that the thickness of the condensed-phase material (C-layer) increases with increasing substrate exposure time. This increase in thickness is corroborated by EDX analysis, as substrate exposure time is increased, the peaks of Cr, Fe, and Ni gradually disappear (**Figure 8(a5-c5)**). This is due to the fact that electrons from the EDX bombardment are able to reach the surface of the SS substrate as the C-layers formed at the lower substrate-flame interaction times are thinner. Similar to the C-layers collected at various flame heights, the mass of the soot layer did not play an

impactful role in the hydrophobicity of the soot layer. The variation of substrate exposure time created C-layers with large differences in mass, however, the CAs for the created layers were very similar (**Figure 8(a2-c2)**). The C-layers produced at the three substrate exposure times shared similarities in their morphologies, physical characteristics and a hierarchical structure. HR-SEM imaging shows that the condensed-phase deposits are formed from agglomerated spherical nanoparticles fused together to form long chains (**Figure 8(a4-c4)**). The EDX data collected on the C-layers formed at substrate exposure times of 2, 5 and 10 minutes shows O contents of 0.46 at.% (**Figure 8(a5)**), 1.42 at.% (**Figure 8(b5)**) and 2.43 at. % (**Figure 8(c5)**), respectively.

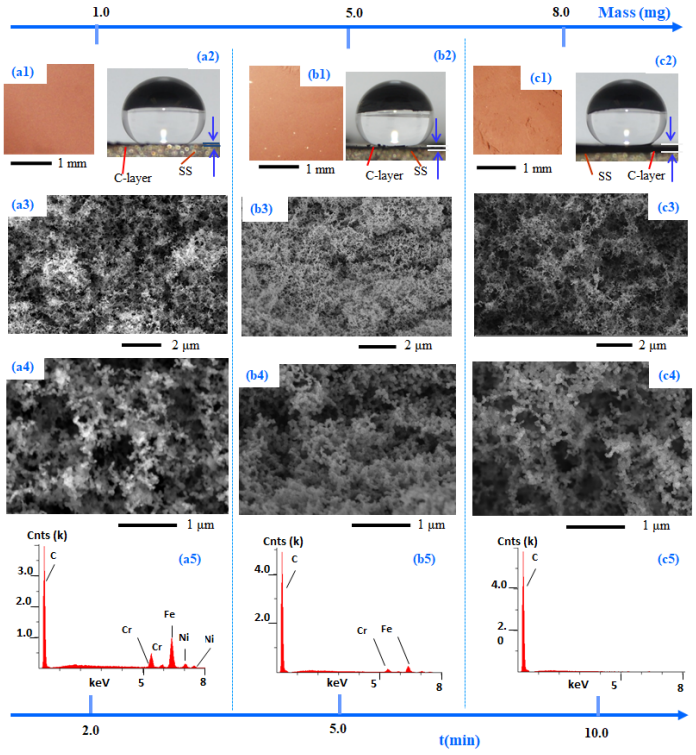

Figure 8. *Hydrophobic surfaces formed on the surface of SS substrates inserted in a CME/air diffusion flame under substrate exposure times of 2, 5 and 10 minutes at a fixed HAB of 15 mm. SEM images show morphological details of the surface. The photographs show that all C-layers are hydrophobic. The EDX spectra show the bulk chemical composition of the C-layers.*

The EDX spectra show that the C content for the 2, 5, and 10 minute exposure times are ~96.06 at.%, 97.62at.% and 97.50 at.%, respectively. Comparing the EDX profiles of **Figure 8(a5)** to **Figure 8(c5)**, it is shown that C contents remain approximately constant. However, the atomic percentage of O increases slightly with time. We do not expect that such a small change can make a significant impact to the layer quality and the CA formed. Our EDX analysis agrees with the work of Saito et al. who conducted unique flame material/soot deposition experiments to establish the history of the soot particle (morphological and chemical characteristics) from flames formed using various types of fuels. The flames were probed at various axial distances from the burner port. Saito et al. reported the physical and chemical soot characteristics in nine different hydrocarbon fueled diffusion co-flow flames including: methane; ethane; acetylene; propane; allene; 1-butene; 1,3 butadiene; and benzene with air as the oxidizer [83]. Using electron spectroscopy for chemical analysis (ESCA) it was found that the clusters of the soot primary particles deposited on the solid support had both adsorbed oxygen and oxygen chemically bound to carbon. The history of soot particles was also studied by varying the substrate's exposure time. The substrates were inserted in the flame for 2, 3, 5, and 8 minutes in a methane flame. However, it was found that ESCA results were nearly the same for all four sampling times.

3.3 Chapter Summary

In this chapter a CME/air co-flow flame was used to create various hydrophobic C-layers on a stainless steel substrate. SS substrates were inserted into the CME/air flame (total height of 22 mm) at heights of 10, 12, 15, and 20 mm for an exposure time of 5 minutes. The C-layer formed at an insertion height of 10 mm (height of the inner flame cone) was the only layer that showed

hydrophilic properties. The formed deposits at 10 mm HAB were irregular and granular-like in structure. However, the remaining flame heights produced hydrophobic and superhydrophobic deposits that all shared branching and web-like structures of varying complexity. When the substrates were inserted into the CME/air flame at an insertion height of 15 mm for an exposure time of 2, 5, and 10 mins the layers produced were all hydrophobic and showed surface structures consisting of branching and web-like structures.

Chapter 4: CH_4/Air Flame Formed Hydrophobic Layers[4]

4.1 Impact of Methane/Air Flame Structure on the Synthesis of Hydrophobic Surfaces

In order to support our hypothesis that flame structure is an important factor in the synthesis and properties of the C-layers, a CH_4/air flame was used to generate C-layers. SS disks were introduced within the methane/air flame at two heights: one region within the flame "inner-cone" and the other in the luminous zone ("outer-cone" region) as shown in the flame schematic in **Figure 6**. There is a significant structural variation between the flame formed using CH_4 and CME. The CH_4/air flame is much taller compared to the CME/air flame and results in a larger variation of the soot morphology. The CH_4/air flame has longer asymmetric regions for soot formation compared to the CME/air flame. Additionally, the carbon particulate propensity is much stronger in biodiesel flames. SS disks of matching physical and chemical characteristics as those used in the CME/air flame were used for this set of experiments. The SEM images in **Figure 9** show the typical morphology of the condensed-phase deposits on the surface of SS disks positioned at various flame heights in the CH_4/air flame (HAB = 50 and 60 mm) with a substrate exposure time of 1 minute. SEM analysis on the surface of the condensed-phase deposits reveal that the size, shape, and degree of particle agglomeration is strongly dependent on the flame position. The SS substrate inserted at a HAB of 50 mm appears to have two deposition zones. One is an outer ring of a "darker" contrast surrounding a circular inner layer of "light" contrast (schematic in **Figure 9(a)**). There is a heavy

[4] The content of this chapter is an extension of a published paper by the author [27, 60], co-authors have granted full authority for the reproduction of the material. The paper contains results of research which was solely conducted as partial fulfillment for the MS requirement. Materials presented in the paper have not been submitted for a course or extra credit.

deposition of the condensed-phase materials at the edges of the disk compared to a much lower deposition at the center (**Figure 9(a1)**).

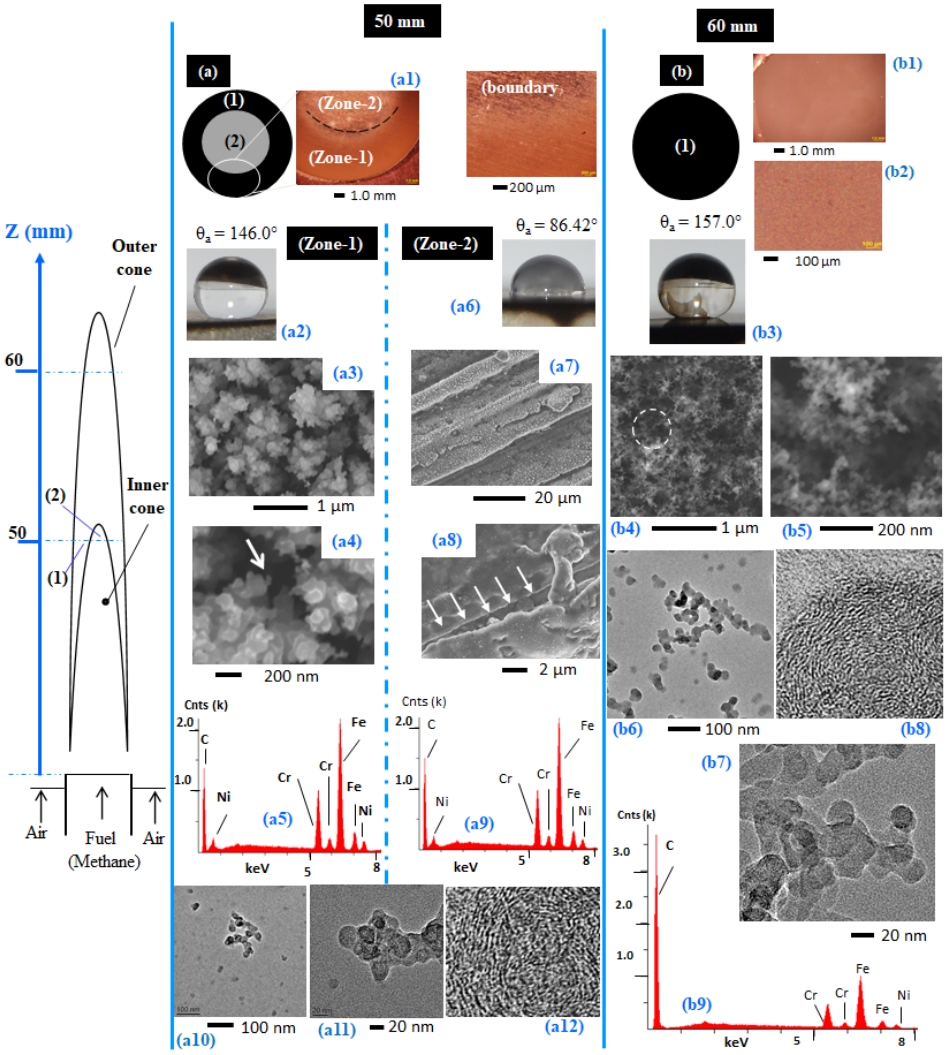

Figure 9. *Morphological history of the C-layers formed on the surface of SS substrates inserted in a CH_4/air diffusion flame at a HAB of 50 and 60 mm for a substrate exposure time of 1 minute. The photographs show the static contact angle of water droplets on the surface of the corresponding layers formed at the two axial distances from the burner port. For TEM analysis, samples of soot particulates were collected thermophoretically by introducing TEM grids near the positions where the SS disks were introduced in the flame. The EDX spectra (a5, a9, b9) show the bulk chemical composition of the C-layers.*

This “ring-like” shape on the surface of the SS disk at the lower regions of the flame correlates well with the shape of the soot volume fraction profiles obtained using light extinction technique in this type of flame [85]. Typical soot volume fraction profiles at the lower part of a co-flow flame have a double “wing-like” shape. As one travels from one side of the flame to the other, a thin luminous flame sheet surrounds the “inner-cone”. The “wing-like” shape present in the soot volume fraction profile is due to the soot propensity in this region of the flame. Therefore, the SS disks have higher quantities of soot deposits on the luminous envelope of the flame, forming the “ring-shaped” C-layers on the outer area of the substrate. The central region of the SS substrate is a lighter contrast due to a very thin coating of carbon deposits; grooves from the polishing of the SS disk can be observed across the SEM images (**Figure 9(a7)**). The two areas of contrasts on the SS substrate inserted at 50 mm HAB in the flame medium, have hydrophobic and hydrophilic characteristics (**Figure 9(a2, a6)**).

A water droplet test shows that the dark contrast “ring” deposition region is hydrophobic (**Figure 9(a2)**) while the inner disk area (lighter contrast material) is hydrophilic (**Figure 9(a6)**). At 60 mm HAB the CH_4/air flame deposited a uniform C-layer that coated the entire surface of the SS substrate (**Figure 9(b)**). At this flame height (60 mm HAB) the substrate was within the luminous zone of the flame (high soot propensity) which led to the fully formed C-layer that displayed a hydrophobic CA. Furthermore, SEM analysis shows that at 60 mm HAB the carbon deposits are formed of soot aggregates (long chain-like structures) similar to those found in the hydrophobic layers of the CME/air flames. Within hydrophobic regions of the soot layer at HABs of 50 and 60 mm the soot has a hierarchical structure (**Figure 9(a3, b4)**). A simple visual inspection of inserted

SS disks at various axial positions in the CH_4/air flame showed that most of the deposits contained a "ring-shape" indicating the annular nature of the flame. The "inner-cone" in the CH_4/air flame extends beyond one half of the flame length (schematic **Figure 6**). However, the surface of the SS disks inserted in the biodiesel/air flame (for all tested HABs except 10 mm) did not contain the "ring-shaped" structure, rather the C-layer coated the metal's surface uniformly (**Figure 7**). SEM analysis revealed that the morphological microstructure variation in a "ring-shaped" C-layer is significant (**Figure 9(a3, a8)**). Through the CH_4/air flame it was found that introducing the SS disk below the tip of the "inner-cone" (~ 40 mm HAB) produced C-layers comprised of deposits similar to those present on "zone-2" of the 50 mm sample. C-layers on SS disks inserted at lower HABs did not contain a significant deposition of the condensed-phase materials, which resulted in the SS substrate retaining its hydrophilic properties. These findings demonstrate the importance of inserting substrates within the luminous region of the flame to effectively generate smooth, continuous, and uniform hydrophobic C-layer coatings on solid substrates.

4.2 Comparison of CH_4/Air and CME/Air Flame Structure and Impact on Synthesized Hydrophobic Layers

It is well established in the literature that combustion of heavier hydrocarbon compounds, such as biodiesel, tends to produce high quantities of soot compared to lighter hydrocarbon fuels such as methane. It was found that the soot volume fraction peak (fv) value for the B100CME/air flame is approximately 11 times higher than the fv peak reported by Lee et al. for a CH_4/air flame using the same burner configuration [85, 67]. This reflects the soot propensity of biodiesel compared to methane and compliments the uniformity of C-layers formed by a CME/air flame versus those

formed by a CH_4/air flame. Similar to the CME flame, soot samples were also collected thermophoretically from the methane/air flame for TEM analysis. **Figure 9(a10-a12)** and **Figure 9(b6-b8)** are representative of the soot morphology collected thermophoretically from the axial region of the flame at HAB of 50 and 60 mm. A simple comparison of the HR-TEM images in **Figure 9(a12, b8)** shows that the inner structure of the soot does not play a major role in the hydrophobicity of the C-layers.

It is very interesting to note that for both CME/air and methane/air flames the introduction of a SS disk within the flame "inner-cone" (pyrolysis zone) results in deposits of nonhomogeneous morphology (radially). The overall flame length of the methane/air ($Z \cong 85$ mm) is significantly larger compared to that of the CME/air ($Z \cong 22$ mm) flame. Relatively, the flame "inner-cone" is much smaller in the CME/air flame compared to the methane/air. Regardless of the fuel type used to form the co-flow flame (CME or methane) the introduction of a SS disk in the flame "outer-cone" or "luminous" zone results in heavy soot deposition and a visible single contrast black C-layer. Additionally, the deposits are of uniform morphologies (radially) (**Figure 7(b-d)** and **Figure 7(b4)**). Conversely, the introduction of a SS disk within the flame "inner-cone" in both flames resulted in two deposition zones of a "light" and "dark contrast" composed of structures of nonhomogeneous morphology (radial); although the presence of the two distinct zones on the surface of the SS disk is more pronounced in the methane flame. The distinction between nonhomogeneous deposits formed in the flame's "inner-cone" (pyrolysis zone) and homogeneous deposits formed in the "outer-cone" (luminous zone) indicate that radial changes in C-layer are due to the inherent structure of the flame. These results correlate well with trend variation of deposition on wires or cylindrical fibers that have been reported in the literature [84, 86]. For

instance, Shim et al. studied radially the variation of soot morphology deposited on the surface of SiC fibers using a co-flow propane air diffusion flame at various flame heights within the flame "nonluminous" and "luminous" flame zones [84]. In that work it was observed that deposits on the SiC fiber varied depending on where the fibers were introduced in the axial location of the flame. That is, when the SiC fiber was introduced at the lower regions of the flame (within the flame "inner-cone") two visible deposition zones of a light- and dark-contrast were formed on the fiber. SEM analysis was conducted on the SiC fiber as if mapping the physical morphology of the structures formed along the radial direction of the flame. Regions of the SiC fiber exposed to the flame "inner-cone" (light-contrast) had structures with morphology that did not vary significantly and remained homogenous. However, SEM analysis of the thicker deposited area (dark-contrast) showed that the morphology of the structures significantly varied along the surface of the thick deposits when compared to the structures formed in the "inner-cone". Nevertheless, when the SiC fiber was introduced in the upper part of the flame or within the flame "luminous zone" the deposits appeared as a single contrast (dark-contrast) and had uniform morphology along the entire SiC fiber. Analogous to those experiments studying deposition on SiC fiber, in our experiments when a SS disk is introduced within the flame "inner-cone" the thickness of the C-layer is not uniform. Additionally, the morphology of the structures forming the deposits appear to evolve along the radial direction of the flame. However, when the SS disk is introduced within the luminous zone ("outer-cone") the thickness of the C-layer appears to be uniform and contain structures of homogenous morphology.

Furthermore, temperature measurements of the CME/air and CH_4/air flames using the rapid insertion technique [67, 87] show a relationship between the temperature of the flame and the

mass/thickness of the deposited C-layers. The relative axial temperature profiles of the CME/air and CH_4/air flame are presented in **Figure 10(a)**. For the CME/air flame the centerline flame temperature varies from ~488°C just above the burner's mouth (~2 mm HAB) to ~873°C near the flame's tip. For this flame at the lowest (~10 mm) and near the highest (~20 mm) sampling plane a centerline flame temperature of 785 and 873°C was measured, respectively (**Figure 10(a)**). On the other hand, the methane/air flame is much hotter than the CME/air and there is a stronger temperature gradient along the axial flame axis. The centerline flame temperature for this gaseous flame varies from ~740 °C at the flame root (~10 mm HAB) to ~1178°C near the flame's tip (~79 mm HAB). The total flame height of the CME/air flame is ~22 mm while that of the methane/air flame is ~85 mm. The overall length of the CME/air flame is a fraction of the methane/air flame indicating that soot inception, growth and oxidation mechanism are much stronger under this oxygenated fuel flame. **Figure 10(b)** shows that for both CME/air and CH_4/air flames, as the SS substrate is moved to a higher position in the flame (for exposure times of 5 mins) the mass and thickness of the formed C-layer increase. In the set of CME experiments where the C-layers were formed at various axial heights (HAB = 10, 12, 15, and 20 mm) at a fixed exposure time of five minutes the mass difference of the C-layers from the lowest to the highest tested part of the flame varies by 8 mg. However, the flame centerline temperature varied by only 88 °C. When the substrate is held within the CH_4/air flame at a constant HAB and variable exposure times, the C-layer formed initially increases in mass and thickness but decreases as the SS is maintained in the flame for longer substrate exposure times (**Figure 10(c)**). In the methane/air flame for the HAB of 50 and 85 mm (at 1 minute substrate exposure time) the mass varied by 0.2 mg while the flame temperature between these two positions varied by 274°C.

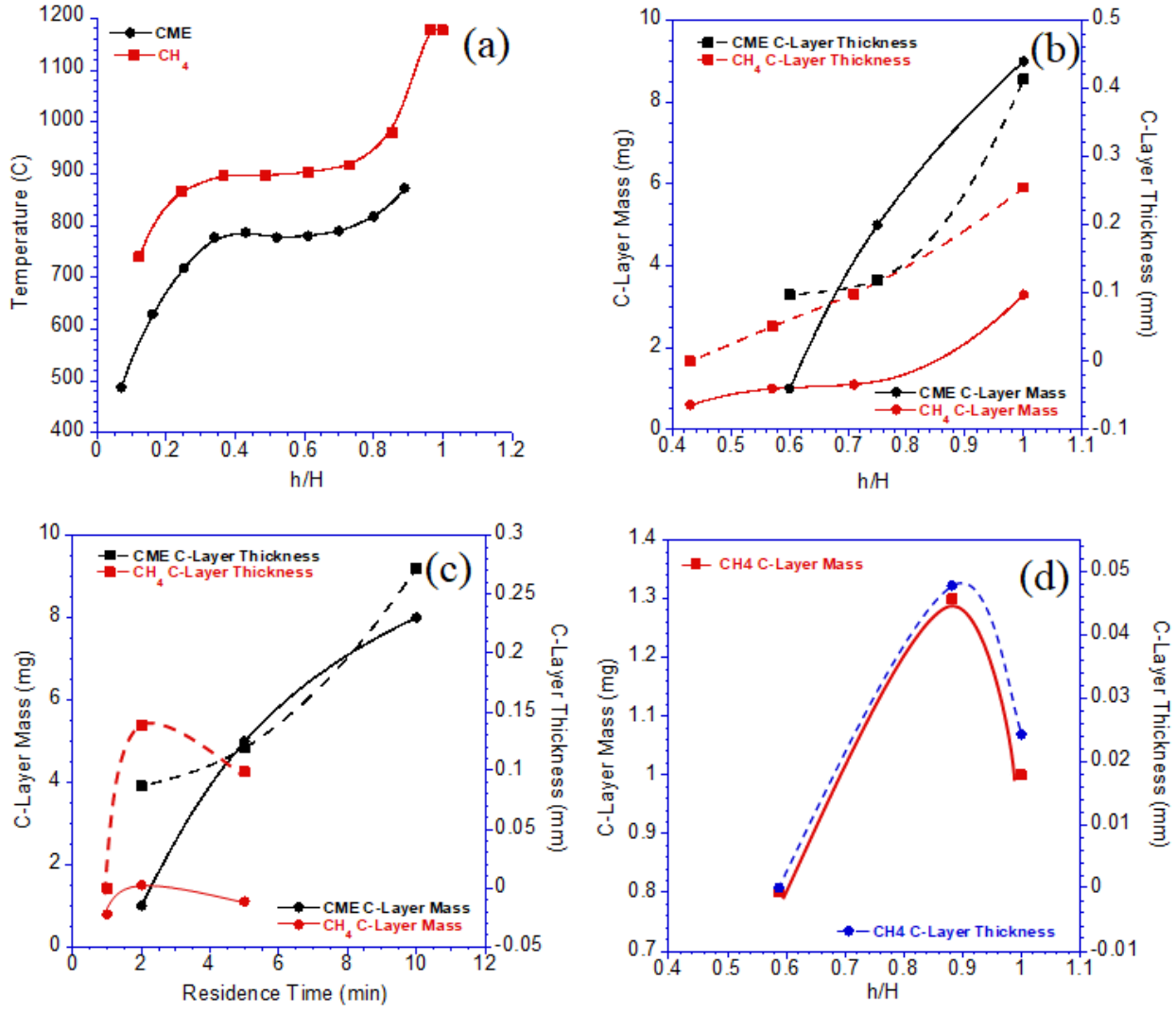

Figure 10. *Several graphs are shown that depict: (a) Relative heights of axial temperature measurements of a CME/air and CH_4/air flame, (b) The mass (mg) and thickness (mm) of C-layers formed on SS substrates from a CME/air and CH_4/air flame at various relative heights for a substrate exposure time of 5 min, (c) The mass (mg) and thickness (mm) of C-layers formed on SS substrates from a CME/air and CH_4/air flame at different substrate exposure times, (d) mass and thickness of a C-layer collected in a CH_4/air flame at various heights for a substrate exposure time of 1 minute.*

We believe the decrease in C-layer mass and thickness is caused by prolonged exposure to high temperatures present in the CH_4/air flame, inducing accelerated oxidation of the soot layer. Oxidation accelerating temperatures are also found to be dependent on the insertion height of the flame. **Figure 10(d)** shows mass and thickness of a C-layer collected in a CH_4/air flame at various heights for a short substrate exposure time of 1 min. Similar to the time dependent experiments, the C-layer's mass and thickness increase, reach a maximum, and finally decrease. The maximum C-layer mass/thickness in **Figure 10(d)** (h/H ≅ 0.9) corresponds to a significant increase in temperature of the CH_4/air flame (**Figure 10(a)**); between h/H values of 0.9 and 1.0 there is a temperature increase of approximately 300 °C. A simple correlation of the temperature profiles with measured masses of the C-layers shows that more soot is being formed in the CME/air flame; this contributes to radiative heat losses, hence cooling the flame to a greater extent. In this context a sootier flame, with lower flame temperatures and with a small "inner-cone" (typical characteristics of a biodiesel flame) appears to be an ideal environment for forming hydrophobic C-layers. EDX analysis was also conducted on the as grown C-layers from the CH_4/air flame as a function of substrate position (HAB of 50 and 60 mm) at a fixed exposure time (1 minute), revealed the presence of carbon, oxygen, chromium, iron, and nickel. (**Figure 9(a5, a9, b9)**). The Cr, Fe, and Ni readings are attributed to the elemental composition of the SS substrate on which the C-layers were formed, while the C reading originates from deposits. The elemental composition at 50 mm HAB on the "zone-1" region is 0.29 at.% O and 86.8 at.% C (**Figure 9(a5)**) compared to 0.71 at.% O and 87.6 at.% C at "zone-2" (**Figure 9(a9)**). The O at 60 mm HAB is 0.73 at.% while carbon is 95.6 at. % (**Figure 9(b9)**). The Cr, Fe, and Ni percentages or peaks in the EDX spectrum decrease significantly at 60 mm HAB where the C-layer gets ticker**.**

4.3 Chapter Summary

In this chapter a CH_4/air flame was used to form C-layers on stainless steel substrates and comparisons between the CME/air and CH_4/air flame were made. SS substrates were inserted into the CH_4/air flame (total height of 85 mm) at heights of 50 and 60 mm HAB for an exposure time of 1 minute. At 50 mm HAB a hydrophobic annular C-layer was produced; the annular geometry of the layer is due to the center of the substrate being inserted into the flame inner-cone and the outer area of the substrate being inserted into the luminous zone of the flame. The hydrophobic deposits at 50 mm HAB had a unique morphology unlike the soot formed in the CME/air flames. At 60 mm HAB the C-layer produced was hydrophobic and uniformly coated the SS disk. Furthermore, the deposited soot at 60 mm HAB displayed web-like branching structures similar to those seen in the CME/air flame.

Chapter 5: CME/Oxygen Enriched Air Flames[5]

The role of oxygen in the formation of soot has been studied by numerous authors [85, 87-91], and it has been found that introducing oxygen into a flame increases the rate of soot inception, formation, agglomeration, and oxidation. These fundamental effects on the flame formed soot may have a profound impact on the structure and hydrophobicity of the flame formed C-layers. In Flame IV and Flame V the effects of oxygen enhanced combustion on deposited carbon films were studied using a CME/oxygen enriched air flame. The SS substrate was inserted into the flame volume at three-quarters the flame height. This relevant insertion height was used due to the overall height of the flame shrinking as oxygen content in the oxidizer stream increased (**Figure 5** and **Figure 6**). Oxygen contents of 21%, 35%, and 50% O_2 were used, with respective substrate insertion heights of 15 mm, 9 mm, and 8 mm (**Table 2**).

At all three O_2 contents the substrate was introduced to the flame's luminous zone and the produced C-layers were hydrophobic (**Figure 11(a1-c1)**). At 35% O_2 the C-layer produced was superhydrophobic (CA = 154°) with a mass of 6 mg, a 1 mg increase compared to the air flame. This mass increase coincides with the increase in soot volume fraction between CME combustion with air and 35% O_2 [67], indicating a greater abundance of soot in the flame. Furthermore, at 35% O_2 the deposited material consists of similar weblike structures that were seen in the CME/air and CH_4/air flames (**Figure 11(b1-b3)**). Once the oxygen content was increased to 50% O_2, the flame deposits were no longer superhydrophobic, producing a hydrophobic CA of 146°. The decrease in

[5] The content of this chapter is an extension of a published paper by the author [27, 60], co-authors have granted full authority for the reproduction of the material. The paper contains results of research which was solely conducted as partial fulfillment for the MS requirement. Materials presented in the paper have not been submitted for a course or extra credit.

the performance of the layers of the hydrophobic material was accompanied with a drop in mass to a low of 1 mg (compared to 5 mg at 21% O_2 and 6 mg at 35% O_2). This correlates well with our previous work on soot formation where it was reported that the soot peak volume fraction of CME/50% O_2 flame was significantly larger than the CME/21% O_2 flame; however, when mass of the total soot was measured, the mass in the 21% O_2 flame was larger than the 50% O_2 flame, indicating that soot is undergoing an oxidation process [67].

Oxidation of deposited soot accounts for the reduction in mass as well as the difference in soot development/structure is demonstrated in the TEM images (**Figure 11(a5-c5)**). The soot formed in the CME/air and CME/35% O_2 appears to be "irregular-shaped" [92], indicated by a lack of distinct shapes or boundaries of the soot, providing evidence that the soot has not yet been fully carbonized (**Figure 11(a4, b4)**). It is evident from the TEM images that there is a gradual decrease in the amount of "irregular-shaped" structures as oxygen is increased from 21% to 35% and finally to 50%.

It is important to note that at all three oxygen contents the hydrophobic portions of the flame formed C-layers share similar branched, weblike, porous structures (**Figure 11(a1-a3, b1-b3, c1-c3)**). This not only demonstrates the flame method's capability to consistently form hydrophobic soot depositions under vastly different conditions, but also emphasizes the importance of these branching hierarchical structures. The hydrophobicity of the current deposited carbon films is due to their surface structure/topography; this is a physical characteristic not a chemical one. Therefore, the unique topography created via soot deposition is the mechanism that facilitates the hydrophobicity exhibited by the deposited C-films.

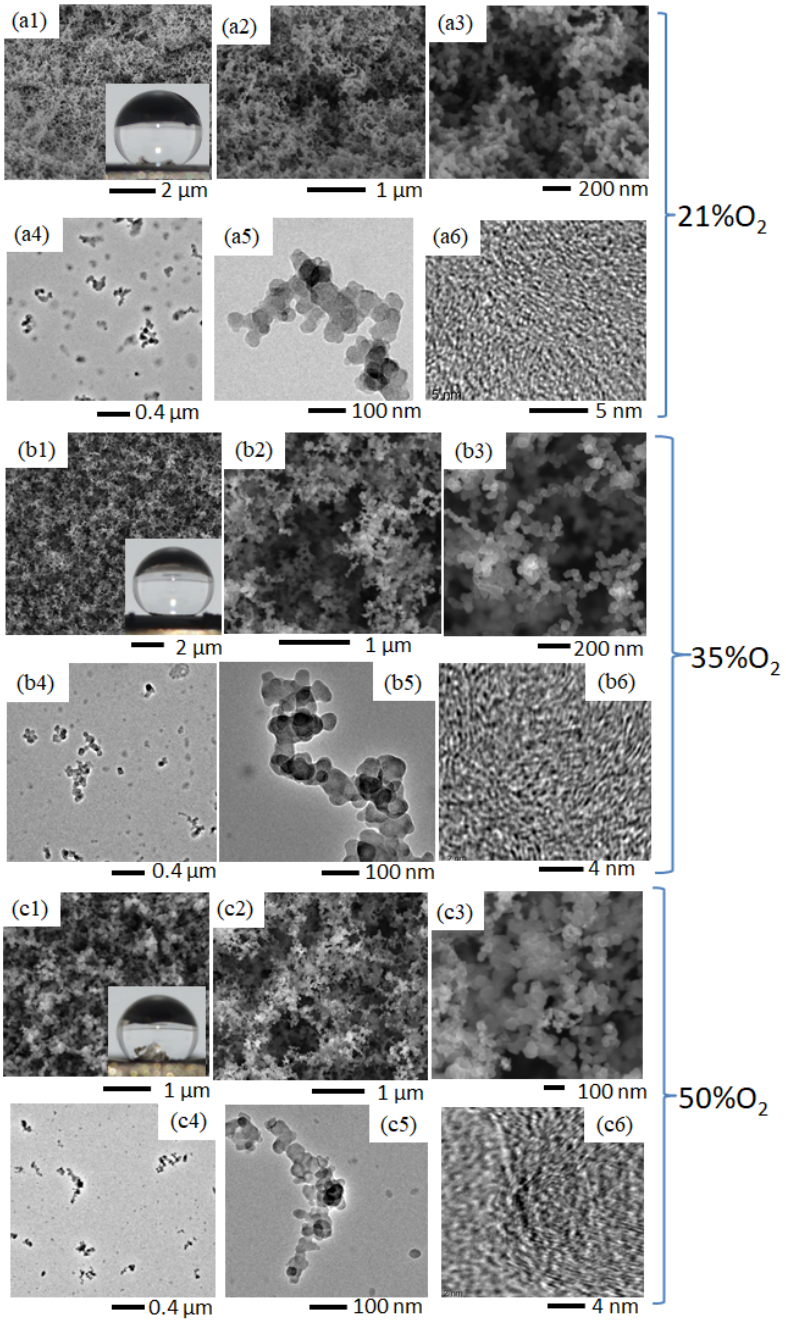

Figure 11. *Comparative SEM images of C-layers formed in a CME/air flame (a1-a3), CME/35% O_2 flame (b1-b3), and CME/50% O_2 flame (c1-c3). TEM images of soot collected at the respective flame insertion heights of the substrate for the CME/air flame (a4-a6), CME/35% O_2 flame (b4-b6), and CME/50% O_2 flame (c4-c6).*

The introduction of increased oxygen in the oxidizer stream prompted the formation of surface cracks on the C-layer (35% and 50% O_2; **Figure 12(b2)** and **Figure 13(b2)**) as well as layer peeling (50% O_2; **Figure 13(a1)**). These surface instabilities were attributed to the increase in temperature that accompanies increased oxygen content during combustion. The CME/air flame at a HAB of 15 mm produced a flame temperature of 788℃. Flame temperature increased to a peak of 938℃ at a HAB of 8 mm when oxygen content increased to 50% O_2. Furthermore, these instabilities occurred at the edge of the C-layer, which corresponds to the edge of the flame (location of flame/oxidizer interaction) where the flame temperature would be highest [93].

5.1 CME/35% O_2 Flame Formed C-Layer

The introduction of an intermediate amount of oxygen in the oxidizer stream (35% O_2) resulted in black sooty film deposits with visible indications of structural instability and non-uniformity. This is evidenced by distinct deposition zones: Region 1 an area of weblike structures bordered by Region 2, an area of compacted soot (**Figure 12(a1-a2, b1-b3)**). These varying deposition areas/zones are created by significant temperature gradients within the flame as well as the thermal stress experienced by the cold substrate interacting with the hot CME/oxygen enriched-air flame.

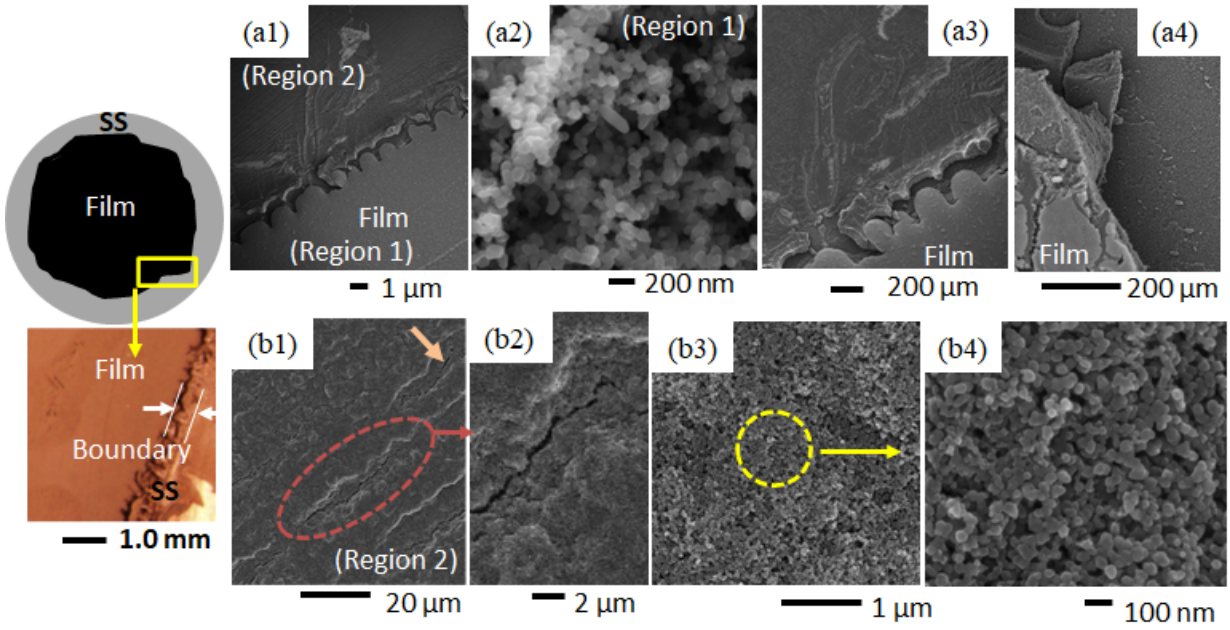

Figure 12. *A diagram depicting soot deposition, light microscopy images of soot deposition, and SEM images of C-layers formed in the CME/35% O_2 flame are shown. At 35% O_2, a light and dark contrast was observed (a1-a4); with the lighter contrast area producing weblike structures (a2) and the area of darker contrast consisting of compacted soot with microscale cracks (b1-b4).*

The deposited film formed at 35% O_2 shows significant modification of its surface morphology compared to the air-counterpart. The deposited carbonaceous film exhibits two different contrasts under the electron beam (**Figure 12(a1)**). A larger inner circular deposition of a "light-contrast" enclosed by a thin outer "darker-contrast" area (Region 1 and Region 2 in **Figure 12(a1)**). HR-SEM imaging of Region 1 reveals that this part of the deposited film is composed of the typical structure of mature soot: deposits are formed of shorter, chain-like structures made up of tens of nearly spherical carbon beads and branched aggregates (**Figure 12(a2)**); this type of morphology is very similar to that found in the CME/air flames. However, the entirety of the deposited C-layer does not share this morphology. Region 1 and Region 2 are clearly separated by a boundary

(**Figure 12(a1, a3-a4)**); higher resolution SEM imaging shows large morphological variations between soot deposits in Region 1 and Region 2.

The carbonaceous deposits on the "darker-contrast" portion of the layer (Region 2) do not display the typical weblike structures, instead it appears as if the particles are joined together, and the agglomerates have been compacted to fill the voids (**Figure 12(b3-b4)**). Further SEM imaging of Region 2 reveals unique structural cracking (**Figure 12(b1-b2)**). These cracks are initial signs of thermal stress/fatigue and while very small (widths < 1 μm) they can be seen at multiple locations across Region 2. Such unique defects are neither observed in Region 1, nor the CME/air flame, nor the CH_4/air flame. We hypothesize that these effects are due to thermal stresses caused by the increase in flame temperature inherent to oxygen enriched combustion. Furthermore, flame temperature increases from the center of the flame to its outer radius, providing an explanation as to why these cracks are only found on the perimeter of the C-layer. As the SS substrate is exposed to the hot flame medium it expands and once removed from the hot flame, with the attached deposits, it cools and contracts; this rapid sequence of expanding and contracting forms small cracks on the deposited C-layer.

5.2 CME/50% O_2 Flame Formed C-Layer

The film formed on the substrate by the CME/50% O_2 flame shows a wide variety of macro and nanoscale morphologies (**Figure 13**), including the weblike interconnected structures that are typical of hydrophobic flame formed carbon deposits; surface cracks and fractures that were first seen in the CME/35% O_2 deposition layer; and unique curled portions of the C-layer that have not

been observed before. These unique morphologies are brought out by the intense temperature conditions of the CME/50% O_2 flame.

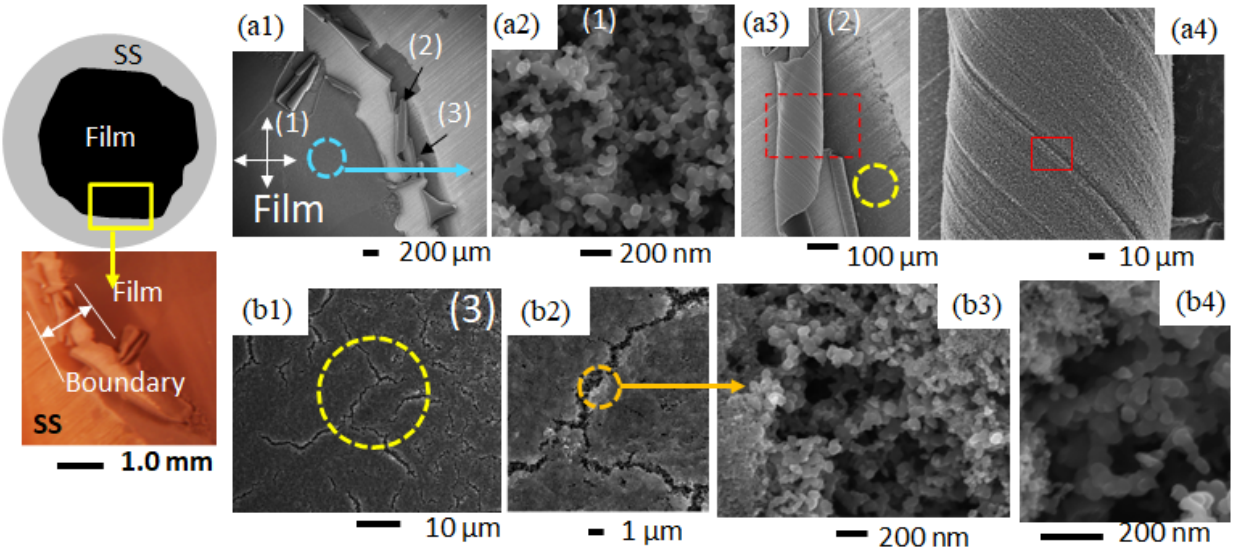

Figure 13. *A diagram depicting soot deposition, light microscopy images of soot deposition, and SEM images of C-layers formed in the CME/50% O_2 flame are shown. Three distinct regions of deposits were formed (a1). The first region is formed by typical weblike structures (a2); the second region is made up of early soot deposits that have been curled (a3-a4); and the third region is comprised of compacted soot that has been significantly fractured (b1-b4).*

As seen in **Figure 13(a1)** there are three distinct morphological regions of the CME/50% O_2 flame formed film: (1) the hydrophobic inner region; (2) the region of curled soot layers; and (3) the uncurled perimeter of the deposited film. Region 1 consists of interconnected carbon spherules that form a weblike structure similar to the morphologies common in the CME/air flame (**Figure 13(a2)**). Region 2 consists of peeling carbon layers that were easily observed even by the naked eye (**Figure 13(a1, a3-a4)**). Curled portions of the deposit have easily visible engraved lines (**Figure 13(a2, a3)**) that correlate to the grooves present on the surface of the SS disk (**Figure**

13(a3)), indicating that the soot exposed by the curls are early deposits. HR-SEM analysis of these early deposits shows interconnected carbon branches similar to those found in Region 1. Region 3 of the film is located at the perimeter of the deposition zone (**Figure 13(a1)**) and can most easily be characterized by the large cracks on its surface (**Figure 13(b1-b2)**). These cracks are significantly larger in size than those found at 35% O_2 and appear in much greater quantity. However, looking within the cracks of the CME/50% O_2 layer using HR-SEM provides great insight into the morphology of early soot deposits. It appears that earlier deposited soot consists of weblike structures comparable to structures found in Region 1 (**Figure 13(b3-b4)**); this is consistent with HR-SEM imaging of the curled layers in Region 2. Additionally, the surface of Region 3 consists of compacted soot spherules that have not formed interconnected weblike structures and are similar to the deposits in the darker contrast of the film formed at 35% O_2 (**Figure 12(b3-b4)** and **Figure 13(b2-b3)**). We believe that these unique morphologies were created by the high temperatures of the CME/50% O_2 flame, specifically at the high temperature area at the edge of the flame where Regions 2 and 3 were located.

Both flames formed in CME/oxygen enriched combustion (35% O_2 and 50% O_2) could produce hydrophobic layers, however there were signs of instability that had not been observed in other flame formed layers. These instabilities occurred at the perimeter of the formed C-layer, where during deposition the flame temperature would be greatest. Both CME/35% O_2 and CME/50% O_2 flame formed layers showed signs of thermal stress induced cracking. Additionally, the CME/50% O_2 layer had areas where the once planar soot began to curl, which provided evidence that early soot deposits consisted of the typical weblike structures. Interestingly, both levels of oxygen enhancement showed similar morphologies of compacted soot spherules near areas of high thermal

stress (**Figure 12(b3)** and **Figure 13(d3)**). This provides evidence that the high temperature areas of the flame are modifying what was once a weblike structure into a compacted bed of nanosoot beads.

5.3 Chapter Summary

In this chapter CME/oxygen enriched-air (35% and 50% O_2) flames were investigated to understand the effect of oxygen on the formation of hydrophobic C-layers on stainless steel substrates. The SS substrates were inserted into the flame volume at three-quarters of the flame height, this relevant flame height was used due to the overall height of the flame decreasing as oxygen content was increased. At both oxygen contents hydrophobic C-layers were formed on the substrate, however, these C-layers contained unique morphologies that showed sign of thermal stresses. At 35% O_2 the flame formed C-layer showed minor signs of thermal stress that consisted of small cracks. At 50% O_2 thermal stresses were much more noticeable in the flame formed C-layer. In addition to more significant cracking (cracking defects of the layer were much larger than at 35% O_2) there were signs of layer peeling that exposed early soot. The thermally induced structural defects of the C-layers formed in 35% and 50% O_2 flames were located at the edge of the C-layer (outer radius of the flame) where flame temperatures would be greatest.

Chapter 6: Nature of Hydrophobicity in Flame Formed C-layers[6]

To better understand the underlying mechanism of the hydrophobicity of the carbon deposits, a series of analyses were conducted on the as-condensed phase materials. It is important to note that regardless of flame structure (i.e., fuel, oxidizer type), regions of the flame are composed of particle nucleation, surface growth, particle coagulations and coalescence, and soot oxidation. A SS substrate inserted in one of these flame regions can have different morphological microstructure variations which play a significant role in the hydrophobicity of the layers.

Our initial hypothesis is that the effect of surface morphology is critical for hydrophobicity of the C-layers rather than the chemical composition or energy state of the material. XPS analysis was conducted to support this initial hypothesis. **Figure 14(a)** shows the wide energy range XPS scans recorded from carbon deposits formed on the surface of SS disks under various conditions after introduction into the flame medium. All scans show two main peaks, one at ~284.3 eV for C 1s core-level states and the second at ~532.6 eV that corresponds to O 1s core-level (**Figure 14(a)**). The XPS analysis shows that the C-layers contain only carbon and oxygen species. **Figure 14(b)** shows narrow-range spectra recorded for C 1s. The spectra labeled as #1 to #4 correspond to C-layers formed in the CME/air flame for a substrate exposure time of five minutes at a HAB of 10, 12, 15 and 20 mm, respectively. The electron lines for the C 1s spectra have a more symmetric shape. Furthermore, the C 1s core level shows no indication of complex surface functional groups (i.e., phenols, carbonyls, carboxylic) and flame position did not influence surface functional

[6] The content of this chapter is an extension of a published paper by the author [27, 60], co-authors have granted full authority for the reproduction of the material. The paper contains results of research which was solely conducted as partial fulfillment for the MS requirement. Materials presented in the paper have not been submitted for a course or extra credit.

groups. Additionally, it appears that the carbon deposits remained the same as the substrate was held for varying periods of time within the flame medium (spectrum # 5 and #6). Spectrum # 5 and #6 are of C-layers formed on the SS disk introduced in the flame at a HAB of 15 mm for 2 and 10 min, respectively.

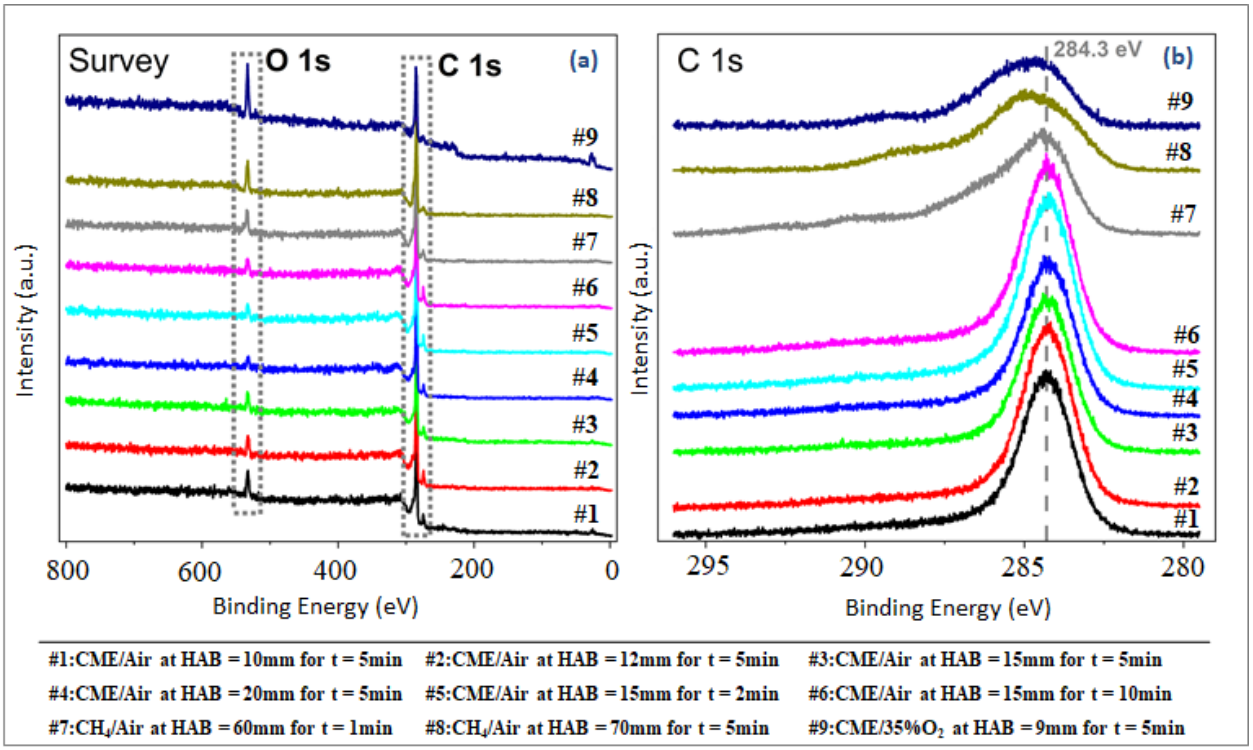

Figure 14. *Results from X-Ray Photoelectron Spectroscopy (XPS) are shown: (a) A wide energy range XPS spectrum recorded from the C-layers formed at various conditions; (b) C 1s spectra recorded from the C-layers.*

Spectrum #7 and #8 are from the carbon deposits from a methane/air flame at HAB of 60 mm (1 min) and 70 mm (5 min). Spectrum #9 is for carbon deposits from a flame formed using CME as a fuel with 35%O_2 + 65%N_2 in the oxidizer stream (air was used in our reported results) for a

substrate exposure time of 5 min at HAB ~9 mm. The oxygen enhanced flame condition (spectrum #9) was tested to illustrate the effect that an oxygen enriched-air flame may have on the state of the carbon particulates forming the deposits. The C 1s peak of the C-layer formed at a HAB of 60 mm (spectrum #7) is asymmetric with more weight at lower binding energies, meaning that a majority of the contribution to the peak is due to C-C bonds. C 1s peaks for spectra #8 and #9 are more symmetric and broader, therefore the contribution from oxides has increased for these samples. While there are some variations in the carbon oxidation state forming the C-layers, CA analysis show that the hydrophobicity of the C-layers is strongly dependent on flame structure. That is, the uniformity of the physical morphologies of the deposits is highly dependent on whether the SS disk is introduced in the flame's "inner-cone" or "outer-cone".

Figure 15(a1-a6) represents SEM and HR-SEM images collected on the surface of a hydrophobic layer formed in the flame. The C-layer was formed on the surface of a SS disk probed at the tip of the methane flame. **Figure 15(a1)** shows regions of the undisturbed and disturbed film. The disturbed region was created mechanically with a sharp laboratory knife to help visualize the uniformity of the layer. The magnified views (**Figure 15(a2-a6)**) of an undisturbed region of the hydrophobic layer (circled area in **Figure 15(a1)**) reveal that it is composed of carbon aggregates that are very long and of unique fractal morphology. A single carbon aggregate is formed of hundreds of individual smaller primary soot particles (**Figure 15(a5-a6)**). Gaps, voids or empty spaces are formed within the film during the aggregate deposition process (**Figure 15(b2)**). As the mature soot is initially carried by the gas flow it is ingrained within the grooves present on the substrate's surface. As the C-layer continues to grow, new soot aggregates or mature soot are deposited on already existing aggregates creating the gaps and voids (**Figure 15(b2)**). HR-SEM

imaging reveals the high porosity present on the surface of the C-film (**Figure 15(a2-a4)**). The HR-SEM on a typical aggregate shows that particles are in the range of 30 nm (**Figure 15(a6)**). These elongated aggregates and the high density of gaps or voids within the deposited carbonaceous material contributes to the hydrophobicity of the C-layer by forming an ideal hierarchical surface. These surfaces consist of micro and nanoscale roughness which is essential for reinforcing the film of the droplet and maintaining a solid-air-liquid interface [94, 95].

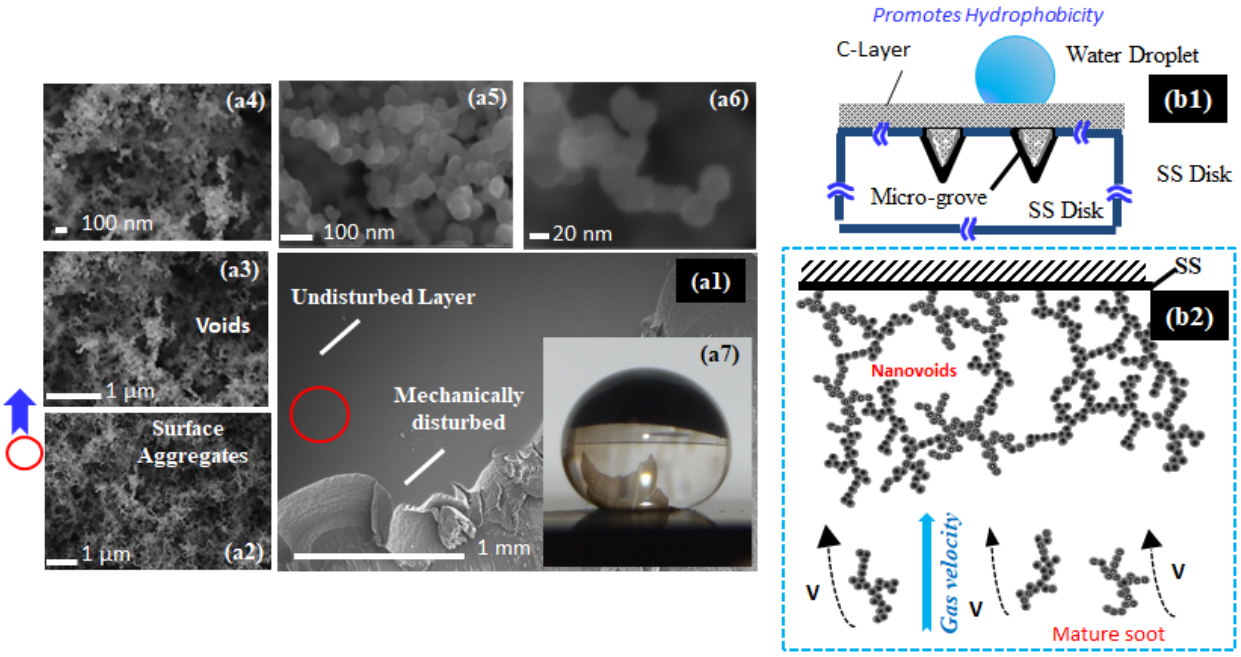

Figure 15. *The mechanism for the hydrophobic soot deposits is shown. (a1-a6) SEM and HR SEM images of the condensate-phase materials on the surface of the SS disk after insertion into the flame are presented. (b1-b2) schematics representing the deposition of soot on the substrate and the hydrophobic C-layer formed.*

The characteristics of the "bulky" condensed-phase materials is that they extrude perpendicularly from the surface of the substrate and that the layer is nonuniform. Similarly, the earliest deposits from the methane and CME flames appear as irregular "bulky" shaped objects or large soot

"globules" composed of individual spheres (**Figure 16(a4)**). It was noticed that the morphology of the deposits significantly varied from location to location on the hydrophilic surface. HR-SEM imaging of the square area in **Figure 16(a1)** contains structures that are smaller in size and less dense (**Figure 16(a5, a6)**). These irregular "globule" structures present on the SS disks probed at the lower regions of the flames produce minimal nanoscale surface roughness, and hence do not promote hydrophobicity in the carbonaceous films. Regions of incipient particles (young soot or soot precursors) are dominant at the lower regions in a co-flow flame [96]. The detailed studies on the formation of incipient soot in co-flow CH_4/air flames by Smyth et al. clearly reveal that initial formation occurs in a region where intermediate hydrocarbons are abundant [97]. Regardless of the phase of the soot particles the young soot displays very rapid mass growth via radical and/or ion reactions [97]. The deposition process or C-deposits at the lower part of the flame involves mostly incipient particles or "young soot" which are transported by the gas flow in the direction of the flame's tip (**Figure 16(b2)**). Deposits are initially formed at the edges of the grooves present on the surface of the SS substrates. The C-deposits at a lower flame height follow particle-particle deposition or nucleation by the rapid and continuous influx, thus giving rise to larger "globule" structures (**Figure 16(b2)**). Similar "globule-like" structures have been reported by Saito and coworkers using various hydrocarbon diffusion flames generated by a co-flow reactor [87]. The work of Saito and coworkers confirmed that soot inception begins with a very small nuclei that can rapidly agglomerate.

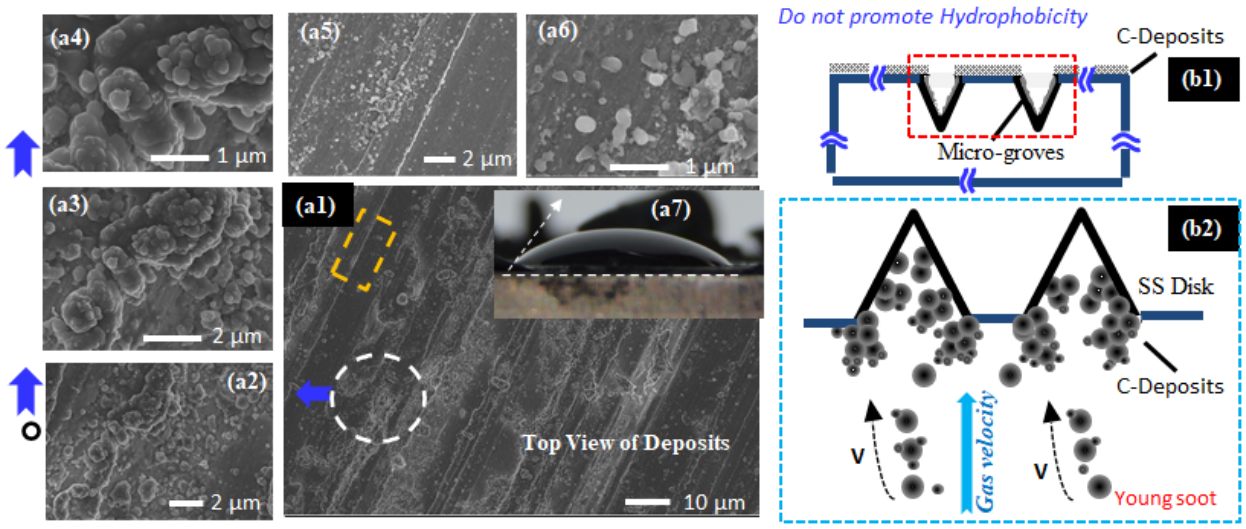

Figure 16. *The mechanism for the hydrophilic soot deposits is shown. (a1-a6) SEM and HR SEM images of the condensate-phase materials on the surface of the SS disk after insertion into the flame are presented. (b1-b2) schematics representing the deposition of soot on the substrate and the hydrophilic C-layer formed.*

6.1 Wettability Properties of the Flame Formed C-Layers

The role of the wettability (Wenzel Equilibrium state vs. Cassie-Baxter Equilibrium state) in hydrophobic surfaces is crucial in the design of new technologies. For instance, hydrophobic surfaces in the Cassie-Baxter equilibrium state are used in heat exchangers to prolong the dropwise condensation effect and to prevent film condensation [9]. The wetting ability of a liquid is a function of the surface energy of the solid-gas interface (nanovoids filled with air), the liquid-gas interface (droplet and gas in the nanovoids), and solid-liquid interface. We hypothesize that water droplets resting on a hydrophobic C-film in our samples exist in the Cassie-Baxter state, as the gaps in the hierarchical structure of the carbon layer are too small to break the droplet's surface

tension. Depictions of the Cassie-Baxter and Wenzel wetting states in the context of the hydrophobic flame formed surfaces are shown in **Figure 17**.

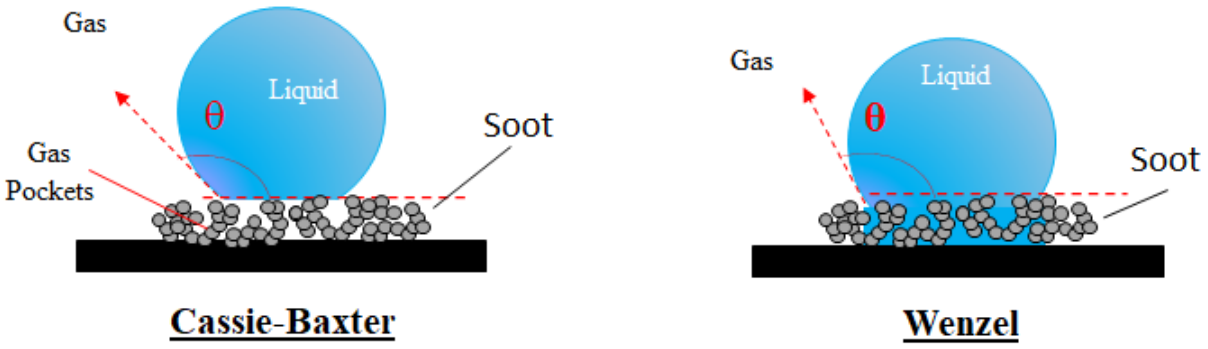

Figure 17. *Illustrations of the Cassie-Baxter (non-wetting) and Wenzel (wetting) states in relation to the flame formed hydrophobic C-layers.*

This hypothesis is supported by the water droplet drop test (WDDT) conducted by releasing a millimetric droplet onto the SS disk coated with flame formed hydrophobic C-layer and allowing the droplet to bounce (**Figure 18**). **Figure 18** is a set of chronological photographs obtained using a high-speed camera (MotionPro X3) on a biodiesel generated C-layer. Images of a falling droplet were collected at 2000 fps through the MotionPro software. As shown in the photo images, just prior to impact (t=0 sec), the droplet has a perfect spherical shape. Upon impact the droplet first deforms, then retracts (flattened shape), bounces off the surface (at which point the droplet is far from spherical), and finally leaves the surface approximately spherical. The droplet continues to bounce off the C-layer a few more times before rolling off the coated disk. The WDDT was also conducted on the hydrophobic C-layers formed in the CH_4/air flame and exhibited similar wettability property as the C-layer formed in the CME/air flame. Dynamic effects of bouncing water droplets were studied extensively by Jung and Bhushan [98]. According to their work, water droplets behave differently depending on whether they exist in the Cassie-Baxter or Wenzel state. Their results showed that in the Wenzel state the water impacting the surface becomes pinned and

fails to completely rebound, instead, it simply stretches and oscillates without leaving the surface until it comes to rest. Under the Cassie-Baxter state, however, the water droplet does not wet the surface and thus the droplet is free to bounce. Novel carbon materials such as carbon nanotubes (CNTs) (single and multiwalled) have been proposed to facilitate the development of hydrophobic surfaces on solid supports with similar nonwetting properties as our flame's carbonaceous deposits [99-101]. CNT orientation, alignment, arrays, forests, and other micro arrangements of the nanotubes are some features needed to promote such wettability behavior. Some of the techniques for synthesizing these novel carbon NMs are complex and composed of multi-step processes. The work of Zhang and coworkers showed that single walled carbon nanotubes (SWCNTs) produced in a CVD method can be synthesized in a variety of microarrangements to finetune the nonwettability properties [99]. However, as shown in this study, hydrophobic surfaces with non-wettability properties can be formed by a biodiesel flame in a single step rapid process in as little as 2 minutes.

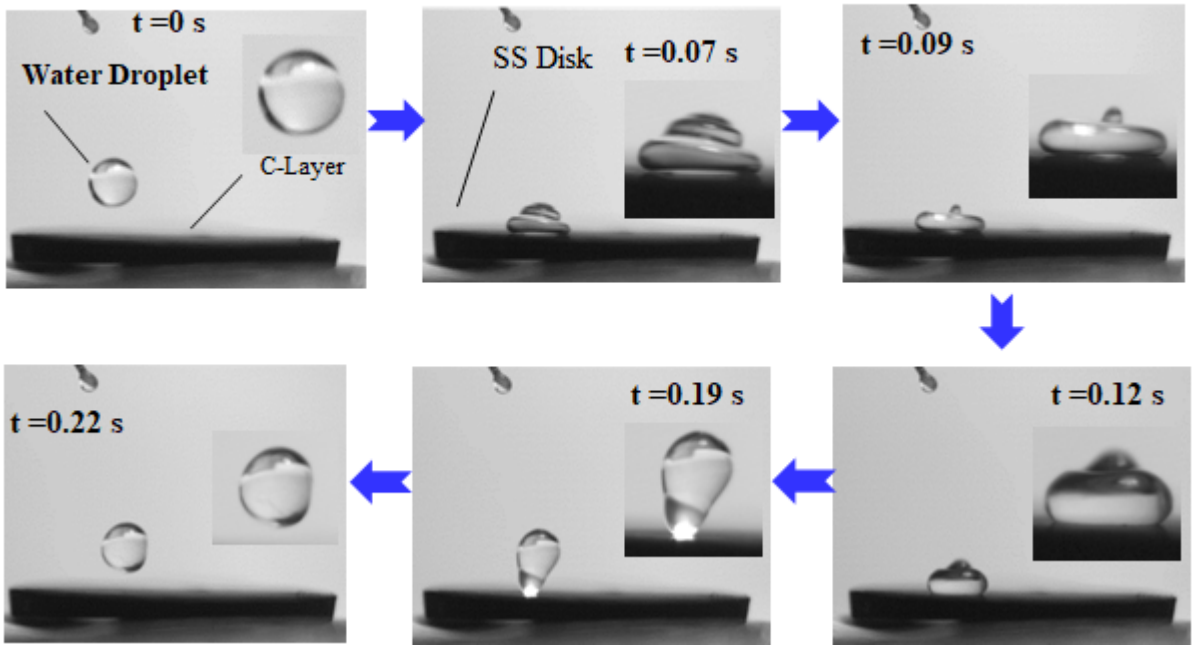

Figure 18. *A set of chronological photographs of a water droplet falling, impacting, deforming, and rebounding during a droplet test on a substrate coated with carbon particulates from a CME/air diffusion flame.*

6.2 Chapter Summary

In this chapter a mechanism for the deposition of hydrophobic C-layers is discussed as well as the wettability properties of the formed layers are presented. The hydrophobicity of the formed C-layers is not chemical in nature and is instead based on the unique surface morphology of the layer. The C-layers are formed by the deposition of a multitude of soot aggregates that eventually form a rough layer. These soot aggregates, when densely packed together, form a porous surface consisting of nanoscale and microscale voids/air pockets. When a water droplet is placed on this

type of material, the micro and nanoscale architectures allow the water droplet to maintain its shape via an interaction formed by the soot, air (trapped within the voids), and the water's surface tension. Furthermore, the wettability characteristics of the C-layer are discussed. It is determined that the C-layers are of the Cassie-Baxter wetting state and that water droplets will not adhere to the material's surface, instead rolling or bouncing off the material.

Chapter 7: Concluding Remarks

7.1 Conclusion

A single-step flame synthesis method to form hydrophobic C-layers directly on stainless steel substrates using a co-flow burner is presented. A variety of flame parameters and configurations (fuel type, flame position, substrates exposure time to the flame, and oxygen content of the oxidizer) were used to analyze different flame formed C-layers. Analysis included water contact angle analysis to determine hydrophobicity; LM and SEM imaging to analyze surface characteristics of the layer; TEM imaging characterize soot stage of growth; EDX analysis to determine element composition of the layer; and XPS analysis to help understand the mechanism underlying the hydrophobic properties of the layer.

Flames were formed using vaporized CME (biodiesel) and methane gas. CME flames utilized oxidizer oxygen contents of 21%, 35%, and 50%; while methane flames solely used air as the oxidizer. Substrates, 19 mm stainless steel (SS) disks, were inserted into the flames at various HAB. Our results show that the biodiesel-air flame represents a more ideal medium to form the hydrophobic carbon layers. The set of experiments in which substrate exposure time was fixed and flame height varied, showed that only a very narrow region of the CME flame (root of the flame or flame “inner-cone”) did not result in hydrophobic surfaces. We hypothesize that a small “inner-cone” of the biodiesel flame along with a high soot propensity can result in an ideal medium to form uniform hydrophobic C-layers. The substrate exposure time experiments (fixed at a single HAB) resulted in C-layers of varying thickness and showed that the mass did not influence the

hydrophobicity (contact angle) of the film coating the SS disk. However, when experiments were repeated using the same experimental setup but with methane the flame regions for forming hydrophobic surfaces were limited. There is a significant structural variation between the flames formed using CH_4/air and CME/air. The CH_4/air flame is much taller (~85 mm) compared to the CME/air (~22 mm) resulting in large variation in the soot morphology. That is, the carbon particulate propensity is much stronger in the biodiesel flame. Moreover, it is interesting to note that regardless of the type of fuel used, carbonaceous deposits formed of aggregates composed of a high degree of primary particle agglomeration tended to promote hydrophobicity. It was also found that, regardless of the fuel type, carbon deposits composed of large "irregular" structures or "globules" do not promote hydrophobicity. A flame region that produced carbonaceous deposits with such characteristics in the biodiesel flame is very small compared to the methane fueled flame.

Changing the amount of oxygen used in the CME flame produced dramatic changes in the flame structure; the most significant of which was a reduction in flame size, impacting the rate of soot formation and growth. Under these conditions there were significant changes to the deposited C-layer mass, degree of hydrophobicity, stability, and surface structure. Increasing the O_2 content from 21% O_2 to 35% O_2 showed changes in surface stability and morphology of the deposited film. At 35% O_2 the first instances of thermal stress and cracking were observed as well as highly compacted spherical soot deposits. The fracturing and compacting of deposited soot occurred on the perimeter of the deposition area, which correlates to the increased temperature region of the CME/35% O_2 flame. When increasing the oxygen content in the oxidizer stream to 50% there was a further decrease in C-layer mass, stability, and hydrophobicity. The mass dropped to a low of 1 mg and the C-layer's hydrophobicity deteriorated. The stability of the film was severely impacted

as this deposition marked the first occurrence of instabilities that could be viewed macroscopically: C-layers were curled at the perimeter of the deposition zone. Using SEM imaging it was determined that the C-layer was cracking and that these cracks were significantly larger than those found in the CME/35% O_2 flame. The instability and cracking of the C-layer at 35% O_2 and 50% O_2 is attributed to the thermal stresses caused by heightened flame temperatures of oxygen enriched combustion.

Across all flames tested it was found that C-layers formed in the outer-cone are uniform and hydrophobic. The flame structure (inner-cone vs. outer-cone) varied by the type of fuel and concentration of oxygen used to form a flame. The C-layers formed in the oxygen enhanced flames exhibit unique structural defects that include a smaller deposition region, peeling of deposits, and cracking at the edges of the films.

X-ray energy dispersive spectroscopy analysis showed that while there are some variations in the carbon oxidation state forming the C-layers, the hydrophobicity of the C-layers was not significantly impacted by chemical differences of the surface. Rather, the hydrophobicity of the C-layer is strongly dependent on where in the flame the SS disk is introduced (flame “inner-cone” or “outer-cone”). The non-wettability state of the C-Layers was verified by performing a water droplet drop test (WDDT). The WDDT showed that the C-layers exist in the Cassie-Baxter state, as the gaps in the microstructure of the carbon layer are too small to cause the droplet’s surface tension to break. HR-SEM analysis on the surface of the “as-grown” C-layer shows that they are composed of long chain-like aggregates formed of primary particles in the nanoscale range. The continuous deposition of these elongated aggregates on the surface creates nanogaps or voids

within the deposited carbonaceous material. These unique features/characteristics contribute to the hydrophobicity of the C-layer by forming an ideal hierarchical surface roughness essential for reinforcing the water film of the droplet.

7.2 Recommendation for Future Research

Future research into the use of flames for hydrophobic synthesis should aim to refine and improve control of soot deposition as well as finding unique methods to enhance properties of flame formed hydrophobic C-layers.

As shown in this work, it is possible to form hydrophobic C-layers on a SS substrate across a variety of flame parameters. Further steps should be taken to refine this method so that layers with specific properties (soot structure, layer mass, hydrophobicity, etc.) can be formed on demand. This would take extensive experimentation involving the adjustment of flame parameters (fuel type, oxidizer, flow rates, etc.), however, this could lead to a type of "handbook" that industries could reference in the future to form hydrophobic layers specific to their needs.

Another avenue for future research would be enhancing, or even adding, properties to the flame formed hydrophobic layers. Some researchers, such as Xiao et al., Feng et al., Zhang et al., and Tan et al. [37, 61-63], have described different methods to enhance flame deposited soot to create layers that are scratch, corrosion, and bacteria resistant. Many of these methods involve applying a polymer layer over the deposited film to serve as protection. With the advancement in polymers and polymer deposition techniques hydrophobic layers that are "smart", conductive, highly

durable, etc. could be produced. Additionally, it may be feasible to sputter coat the flame treated surface with metal. This may provide a highly durable hydrophobic C-layer at a relatively low cost which may be very attractive for certain industrial applications.

Chapter 8: References

[1] Wenzel RN (1936) Resistance of solid surfaces to wetting by water. Ind. Eng. Chem. 28(8):988-994.

[2] Cassie ABD, Baxter S (1944) Wettability of porous surfaces. Transaction of the Faraday Society 40:546-551.

[3] Patankar NA (2004) Mimicking the lotus effect: influence of double roughness structures and slender pillars. Langmuir 20(19):8209-8213.

[4] Pozzato A, Zilio SD, Fois G, Vendramin D, Mistura G, Belotti M, et al (2006) Superhydrophobic surfaces fabricated by nanoimprint lithography. Microelectronic Engineering 83(4-9):884-888.

[5] Sethi SK, Manik G (2018) Recent progress in super hydrophobic/hydrophilic self-cleaning surfaces for various industrial applications: A review. Polymer-Plastics Technology and Engineering 57(18):1932-1952.

[6] Chermahini SH, Ostad-Ali-Askari K, Eslamian S, Singh VP (2018) Recent progress in self-cleaning materials with different suitable applications. American Journal of Engineering and Applied Sciences 11(2):560-573.

[7] Fortin G (2017) Super-hydrophobic coatings as a part of the aircraft ice protection system. SAE International Technical Paper 2017-01-2139.

[8] Lin Y, Chen H, Wang G, Liu A (2018) Recent progress in preparation and anti-icing applications of superhydrophobic coatings. Coatings 8(6):208-241.

[9] Chavan S, Cha H, Orejon D, Nawaz K, Singla N, Yeung YF, et al (2016) Heat transfer through a condensate droplet on hydrophobic and nanostructured superhydrophobic surfaces. Langmuir 32(31):7774-7787.

[10] Puliyalil H, Filipič G, Cvelbar U (2015) Recent Advances in the Methods for Designing Superhydrophobic Surfaces. IntechOpen 11:311-335.

[11] Xue CH, Jia ST, Zhang J, Ma JZ (2010) Large-area fabrication of superhydrophobic surfaces for practical applications: an overview. Sci. Technol. Adv. Mater. 11(3):1-15.

[12] Vandencasteele N, Merche D, Reniers F (2006) XPS and contact study of N_2 and O_2 plasma-modified PTFE, PVDF and PVF surfaces. Surf. Interface Anal. 38(4):526-530.

[13] Barshilia HC, Gupta N (2014) Superhydrophobic polytetrafluoroethylene surfaces with leaf-like micro-protrusions through Ar + O_2 plasma etching process. Vacuum 99:42-48.

[14] Kondrashov V, Rühe J (2014) Microcones and nanograss: toward mechanically robust superhydrophobic surfaces. Langmuir 30(15):4342-4350.

[15] Kontziampasis D, Boulousis G, Smyrnakis A, Ellinas K, Tserepi A, Gogolides E (2014) Biomimetic, antireflective, superhydrophobic and oleophobic PMMA and PMMA-coated glass surfaces fabricated by plasma processing. Microelectronic Engineering 121:33-38.

[16] Jiang L, Zhao Y, Zhai J (2004) A lotus-leaf like superhydrophobic surface: A porous microsphere/nanofiber composite film prepared by electrohydrodynamics. Angew. Chem. Int. Ed. 43(33):4338-4341.

[17] Liu J, Huang J, Wujcik EK, Qiu B, Rutman D, Zhang X, et al (2015) Hydrophobic electrospun polyimide nanofibers for self-cleaning materials. Macromol. Mater. Eng. 300:358-368.

[18] Koo SH, Lee SG, Bong H, Kwark YJ, Cho K, Lim HS, et al (2014) Robust multifunctional superhydrophobic organic–inorganic hybrid macroporous coatings and films. Polymer. 55(11):2661-2666.

[19] Huang YX, Wang Z, Hou D, Lin S (2017) Coaxially electrospun super-amphiphobic silica-based membrane for anti-surfactant-wetting membrane distillation. Journal of Membrane Science 531:122-128.

[20] Zhu J, Zhang S, Wang L, Jia D, Xu M, Zhao Z, et al (2018) Engineering cross-linking by coal-based graphene quantum dots toward tough, flexible, and hydrophobic electrospun carbon nanofiber fabrics. Carbon 129:54-62.

[21] Crick CR, Ismail S, Pratten J, IP Parkin (2011) An investigation into bacterial attachment to an elastomeric superhydrophobic surface prepared via aerosol assisted deposition. Thin Solid Films 519(11):3722-3727.

[22] Rezaei S, Manoucheri I, Moradian R, Pourabbas B (2014) One-step chemical vapor deposition and modification of silica nanoparticles at the lowest possible temperature and superhydrophobic surface fabrication. Chemical Engineering Journal 252:11-16.

[23] Yim JH, Rodriguez-Santiago V, Williams AA, Gougousi T, Pappas DD, Hirvonen JK (2013) Atmospheric pressure plasma enhanced chemical vapor deposition of hydrophobic coatings using fluorine-based liquid precursors. Surface and Coatings Technology 234:21-32.

[24] Paxson AT, Yagüe JL, Gleason KK, Varanasi KK (2014) Stable dropwise condensation for enhancing heat transfer via the initiated chemical vapor deposition (iCVD) of grafted polymer films. Advanced Materials 26:418-423.

[25] Popovicheva O, Persiantseva NM, Shonija NK, DeMott P, Koehler K, Petters M, et al. (2008) Water interaction with hydrophobic and hydrophilic soot particles. Phys. Chem. Chem. Phys. 10:2332-2344.

[26] Esmeryan KD, Gyoshev SD, Castano CE, Mohammadi R (2021) Anti-frosting and defrosting performance of chemically modified super-nonwettable carbon soot coatings. J. Phys. D: Appl. Phys. 54:1-19.

[27] Merchan-Breuer D, Murphy E, Berka B, Echeverria E, McIlroy DN, Merchan-Merchan W (2020) Biodiesel flames as a unique pyrolyzing source for the synthesis of hydrophobic carbon films. Carbon Lett. 31:389-406.

[28] Yang L, Fu H, Yang C, Tian W, Wu P, Jiang W (2019) Carbon soot with arbitrary wettability deposited on solid surface by ethanol flame method. Colloids and Surf. A: Physiochem. Eng. Asp. 578:123576.

[29] Esmeryan KD, Castano CE, Mohammadi R, Lazarov Y, Radeva EI (2018) Delayed condensation and frost formation on superhydrophobic carbon soot coatings by controlling the presence of hydrophilic active sites. J. Phys. D: Appl. Phys. 51:055302.

[30] Wan C, Lu Y, Jiao Y, Jin C, Sun Q, Li J (2015) Fabrication of hydrophobic, electrically conductive and flame-resistant carbon aerogels by pyrolysis of regenerated cellulose aerogels. Carbohydr. Polym. 118:115-118.

[31] Cao H, Fu J, Liu Y, Chen S (2018) Facile design of superhydrophobic and superoleophilic copper mesh assisted by candle soot for oil water separation. Colloids and Surf. A: Physiochem. Eng. Asp. 537:294-302.

[32] Shen L, Wang W, Ding H, Guo Q (2013) Flame soot stably deposited on silicone coating possess superhydrophobic surface. Appl. Surf. Sci. 284:651-656.

[33] Naha S, Sen S, Puri IK (2007) Flame synthesis of superhydrophobic amorphous carbon surfaces. Carbon 45:1696-1716.

[34] Mansurov ZA, Nazhipkyzy M. Flame synthesis of superhydrophobic carbon surfaces.

[35] Zulfiqar U, Hussain SZ, Subhani T, Hussain I, Habib-ur-Rehman (2018) Mechanically robust superhydrophobic coating from sawdust particles and carbon soot for oil/water separation. Colloids and Surf. A: Physiochem. Eng. Asp. 539:391-398.

[36] Mazumder S, Ghosh S, Puri IK (2011) Non-premixed flame synthesis of hydrophobic carbon nanostructured surfaces. Proc. Combust. Inst. 33:3351-3357.

[37] Xiao L, Zeng W, Liao G, Yi C, Xu Z (2018) Thermally and chemically stable candle soot superhydrophobic surface with excellent self-cleaning properties in air and oil. ACS Appl. Nano Mater. 1:1204-1211.

[38] Sung YH, Kim YD, Choi HJ, Shin R, Kang S, Lee H (2015) Fabrication of superhydrophobic surfaces with nano-in-micro structures using UV-nanoimprint lithography and thermal shrinkage films. Applied Surface Science 349:169-173.

[39] Dubov AL, Perez-Toralla K, Letailleur A, Barthel E, Teisseire J (2013) Superhydrophobic silica surfaces: fabrication and stability. Journal of Micromechanics and Microengineering 23(12):1-8.

[40] Bico J, Marzolin C, Quere D (1999). Pearl drops. Europhysics Letters 47(2):220-226.

[41] Forooshani HM, Aliofkhazraei M, Rouhaghdam AS (2017) Superhydrophobic aluminum surfaces by mechanical/chemical combined method and its corrosion behavior. Journal of the Taiwan Institute of Chemical Engineers 72:220-235.

[42] Rahman MA, Jacobi AM (2012) Drainage of frost melt water from vertical brass surfaces with parallel microgrooves. International Journal of Heat and Mass Transfer 55(5-6):1596-1605.

[43] Rahman MA, Jacobi AM (2015) Experimental study on frosting/defrosting characteristics of microgrooved metal surfaces. International Journal of Refigeration 50:44-56.

[44] Arana CP, Puri IK, Sen S (2005) Catalyst influence on the flame synthesis of aligned carbon nanotubes and nanofibers. Proceedings of the Combustion Institute 30(2):2553-2560.

[45] Merchan-Merchan W, Saveliev AV, Kennedy L, Jimenez WC (2010) Combustion synthesis of carbon nanotubes and related nanostructures. Prog. Energy Combust. Sci. 36(6):696-727.

[46] Yuan L, Saito K, Pan C, Williams FA, Gordon AS (2001) Nanotubes from methane flames. Chem. Phys. Lett. 340(3-4):237-241.

[47] Alfè M, Apicella B, Barbella R, Rouzaud JN, Tregrossi A, Ciajolo A (2009) Structure-property relationship in nanostructures of young and mature soot in premixed flames. Proc Combust Inst 32:697–704.

[48] Yuan L, Saito K, Hu W, Chen Z (2001) Ethylene flame synthesis of well-aligned multi-walled carbon nanotubes. Chem. Phys. Lett. 346:23-28.

[49] Vander Wal RL (2000) Flame synthesis of substrate-supported metal-catalyzed carbon nanotubes. Chem. Phys. Lett. 324(1):217-223.

[50] Merchan-Merchan W, Saveliev A, Kennedy LA, Fridman A (2002) Formation of carbon nanotubes in counter-flow, oxy-methane diffusion flames without catalysts. Chem. Phys. Lett. 354(1-2):20-24.

[51] Merchan-Merchan W, Saveliev AV, Kennedy LA (2006) Flame nanotubes synthesis in moderate electric fields: From alignment and growth rate effects to structural variations and branching phenomena. Carbon 44(15):3308-3314.

[52] Saveliev AV, Merchan-Merchan W, Kennedy LA (2003) Metal catalyzed synthesis of carbon nanostructures in an opposed flow methane oxygen flame. Combustion and Flame 135(1-2):27-33.

[53] Vander Wal RL (2002) Fe-catalyzed single-walled carbon nanotube synthesis within a flame environment. Combustion and Flame 130(1-2):37-47.

[54] Gore JP, Sane A (2011) Flame synthesis of carbon nanotubes. In: Yellampalli S. editor. Carbon nanotubes – synthesis, characterization, applications, Intech 7:121-146.

[55] Height MJ, Howard JB, Tester JW, Vander Sande JB (2004) Flame synthesis of single-walled carbon nanotubes. Carbon 42(11):2295-2307.

[56] Pope CJ, Marr JA, Howard JB (1993) Chemistry of fullerenes C60 and C70 formation in flames. J. Phys. Chem. 97(42):11001-11013.

[57] Richter H, Grieco WJ, Howard JB (1999) Formation mechanism of polycyclic aromatic hydrocarbons and fullerenes in premixed benzene flames. Combustion and Flame 119(1-2):1-22.

[58] Alam MS, Shafirovich E (2015) Mechanically activated combustion synthesis of molybdenum silicides and borosilicides for ultrahigh-temperature structural applications. Proceedings of the Combustion Institute 35(2):2275-2281.

[59] Sirignano M, Russo C, Ciajolo A (2020). One-step synthesis of carbon nanoparticles and yellow to blue fluorescent nanocarbons in flame reactors. Carbon 156:370-377.

[60] Merchan-Breuer DA, Murphy E, Berka B, Mendoza Nova LC, Liu Y, Merchan-Merchan W (2022) Synthesis of carbonaceous hydrophobic layers through a flame deposition process. Applied Sciences 12(5):2427.

[61] Feng S, Luo W, Wang L, Zhang S, Guo N, Xu M, et al (2019) Preparation and property of extremely stable superhydrophobic carbon fibers with core-shell structure. Carbon 150:284-291.

[62] Zhang D, Wang L, Qian H, Li X (2016) Superhydrophobic surfaces for corrosion protection: a review of recent progresses and future directions. J. Coat. Technol. Res. 13(1):11-29.

[63] Tan R, Xie H, She J, Liang J, He H, Li J, et al (2019) A new approach to fabricate superhydrophobic and antibacterial low density isotropic pyrocarbon by using catalyst free chemical vapor deposition. Carbon. 145:359-366.

[64] Feng L, Yang Z, Zhai J, Song Y, Liu B, Ma Y, et al (2003) Superhydrophobicity of nanostructured carbon films in a wide range of pH values. Angew. Chem. Int. Ed. 42(35):4217-4220.

[65] Prasai D, Tuberquia JC, Harl RR, Jennings GK, Bolotin KI (2016) Graphene: corrosion-inhibiting coating. ACS Nano 6(2):1102-1108.

[66] Santoro R, Yeh T, Horvath J, Semerjian H (1987) The transport and growth of soot particles in laminar diffusion flames. Combustion Science and Technology 53:89-115.

[67] Merchan-Merchan W, McCollam S, Correa Pugliese JF (2015) Soot formation in diffusion oxygen-enhanced biodiesel flames. Fuel 156:129–141.

[68] Merchan-Merchan W, Sanmiguel SG, McCollam S (2012) Analysis of soot particles derived from biodiesels and diesel fuel air-flames. Fuel 102:525-535.

[69] Fassinou WF (2012) Higher heating value (HHV) of vegetable oils, fats and biodiesels evaluation based on their pure fatty acids' HHV. Energy 45:798–805.

[70] Li TX, Zhu DL, Akafuah NK, Saito K, Law CK (2011) Synthesis, droplet combustion, and sooting characteristics of biodiesel produced from waste vegetable oils. Proceedings of the Combustion Institute 33: 2039–2046.

[71] Knothe G (2005) Dependence of biodiesel fuel properties on the structure of fatty acid alkyl esters. Fuel Processing Technology 86:1059-1070.

[72] Basha SA, Gopal KR, Jebaraj S (2009) A review on biodiesel production, combustion, emissions and performance. Renew Sustain Energy Rev. 13:1628–34.

[73] Song J, Alam M, Boehman AL, Kim U (2006) Examination of the oxidation behavior of biodiesel soot. Combustion and Flame 146:589–604.

[74] Christi Y (2007) Biodiesel from microalgae. Biotechnol Adv. 25(3):294-306.

[75] Dusevich VM, Purk JH, Eick JD (2010) Choosing the right accelerating voltage for SEM (an introduction for beginners). Micros. Today 18(1):48-52.

[76] Pretorius E (2010) Influence of acceleration voltage on scanning electron microscopy of human blood platelets. Microsc. Res. Tech. 73:225-228.

[77] Egerton RF (2014) Choice of operating voltage for transmission electron microscope. Ultramicroscopy 145:85-93.

[78] Amelinckx S, Van Landuyt J (2001) Transmission electron microscopy. Encyclopedia of Physical Science and Technology 53-87.

[79] Zhou W, Apkarian R, Wang ZL, Joy D (2006) Fundamentals of scanning electron microscopy (SEM). In Scanning Microscopy for Nanotechnology; Zhou, W; Wang, ZL; Springer New York: New York, U.S. p. 1-40.

[80] Hodoroaba VD, Motzkus C, Mace T, Vaslin-Reimann, S (2014) Performance of high-resolution SEM/EDX systems equipped with transmission mode (TSEM) for imaging and measurement of size and size distribution of spherical nanoparticles. Microscopy and Microanalysis 20(2):602-612.

[81] Lee MR (2010) Transmission electron microscopy (TEM) of earth and planetary materials: a review. Mineralogical Magazine 74(1):1-27.

[82] Moulder JF, Stickle WF, Sobol PE, Bomben KD (1992) X-ray photoelectron spectroscopy. In Handbook of X-ray Photoelectron Spectroscopy; Chastain, J; Perkin-Elmer Corporation: Minnesota, U.S., p. 9-29

[83] Saito K, Gordon AS, Williams FA, Stickle WF (1991) A study of the early history of soot formation in various hydrocarbon diffusion flames. Combustion Science and Technology 80(1-3):103-119.

[84] Shim Sung Hoon and Shin Hyun Dong (2002) Transition Morphology of Deposits on SiC Fibers in Propane/Air Laminar Diffusion Flames. Combustion and Flame 131:210–218.

[85] Lee KO, Megaridis CM, Zelepouga S, Saveliev AV, Kennedy LA, Charon O, et al (2000) Soot formation effects of oxygen concentration in the oxidizer stream of laminar coannular nonpremixed methane/air flames. Combustion and Flame 121(1-2):323-333.

[86] Shim SH, Ahn KY, Jeong SH, Keel SI, Shin HD (2004) Study of Deposit Morphology in a Propane Diffusion-flame Under Fuel-rich Conditions. Applied Energy 79:179–189.

[87] Saito K, Williams FA, Gordon AS (1986) Effects of oxygen on soot formation in methane diffusion flames. Combustion Science and Technology 47(3-4):117-138.

[88] Merchan-Merchan W, Sanmiguel S, Saveliev A, McCollam S (2013) Soot formation in oxygen-enhanced combustion. In Oxygen-Enhanced Combustion, 2nd ed.; Baukal Jr., C.E.; CRC Press: Florida, U.S., p. 385-408.

[89] Silva LCP, Wilfinger MM, Murari TB, Filho ASN, Moret MA, Santos AAB (2021) Experimental evaluation of thermal radiation and soot concentration rates for syngas flames in lean condition and oxygen enhanced combustion. Energy Rep. 7:4139-4145.

[90] Beltrame A, Porshnev P, Merchan-Merchan W, Saveliev A, Fridman A, Kennedy L, et al. Soot and NO formation in methane-oxygen enriched diffusion flames. Combust. Flame 124:295-310.

[91] Baukal C, Abdihamzehkolaei A, Jimenez WC, Saveliev AV, Merchan-Merchan W (2020) Flow visualization in an oxy-fuel counter-flow burner. In A Gallery of Combustion and Fire, Baukal, Jr. C., Agarwal A., Olson S., Gollner M., Jacobs T., & Vaccari M., Eds.; Cambridge: Cambridge University Press, England.

[92] Merchan-Merchan W, Abdihamzehkolaei A, Merchan-Breuer DA (2018) Formation and evolution of carbon particles in coflow diffusion air flames of vaporized biodiesel, diesel and biodiesel-diesel blends. Fuel 226:263-277.

[93] Han W, Ya Y, Chu H, Cao W, Yan Y, Chen L (2020) Morphological evolution of soot emissions from a laminar co-flow methane diffusion flame with varying oxygen concentrations. J. Energy Inst. 93:224-234.

[94] Lee E, Lee KH (2018) Facile fabrication of superhydrophobic surfaces with hierarchical structures. Scientific Reports 8, 4101.

[95] Teisala H, Butt HJ (2019) Hierarchical structures for superhydrophobic and superoleophobic surfaces. Langmuir 35:10689-10703.

[96] Leung KM, Lindstedt RP, Jones WP (1991) A simplified reaction mechanism for soot formation in nonpremixed flames. Combustion and Flame 87(3-4):289-305.

[97] Smyth KC, Miller JH, Dorfman RC, Mallard WG, Santoro RJ (1985) Soot inception in methane/air diffusion flame as characterized by detailed species profiles. Combustion and Flame 62(2):157-181.

[98] Jung YC, Bhushan B (2008) Dynamic effects of bouncing water droplets on superhydrophobic surfaces. Langmuir 24(12):6262-6269.

[99] Zhang L, Resasco DE (2009) Single-walled carbon nanotubes pillars: A superhydrophobic surface. Langmuir 25(8):4792-4798.

[100] Sun T, Wang G, Liu H, Feng L, Jiang L, Zhu D (2003) Control over the wettability of an aligned carbon nanotube film. J. Am. Chem. Soc. 125(49):14996-14997.

[101] Lau KKS, Bico J, Teo KBK, Chhowalla M, Amaratunga GAJ, Milne WI, McKinley GH, Gleason KK (2003) Superhydrophobic carbon nanotube forests. Nano Lett. 3(12):1701-1705.